J. Fluid Mech. (1992), *vol.* 237, *pp.* 499–539
Printed in Great Britain

A numerical study of the evolution and structure of homogeneous stably stratified sheared turbulence

By STEVEN E. HOLT[1], JEFFREY R. KOSEFF[1], AND JOEL H. FERZIGER[2]

[1] Environmental Fluid Mechanics Laboratory, Department of Civil Engineering, Stanford University, Stanford, CA 94305-4020, USA

[2] Department of Mechanical Engineering, Stanford University, Stanford, CA 94305-4020, USA

(Received 28 September 1990 and in revised form 11 October 1991)

The structure and evolution of homogeneous stably stratified sheared turbulence have been investigated through direct numerical simulation. In these simulations the primary dimensionless parameter is the Richardson number which measures the relative importance of stratification and mean shear.

For Richardson numbers less than the transition value the Reynolds stress and vertical density flux are down-gradient. Some of the vertical kinetic energy gained indirectly through production is expended in creating potential energy. Included in this shear-dominated regime is the stationary Richardson number at which the turbulent kinetic energy is constant in time although the spectra are evolving. At low dimensionless shear rate the stationary Richardson number increases with increasing Reynolds number.

At the transition Richardson number the maximum anisotropy and energy partition are achieved. For larger Richardson numbers potential energy is released into vertical kinetic energy and the vertical density flux becomes counter-gradient. The associated production reversal enhances the decay rate of the turbulent kinetic energy.

The effects of other dimensionless parameters have been investigated. After initial transients the developed flow is rather insensitive to the presence of significant initial potential energy. An increase in the Schmidt number increases the effect of stable stratification, e.g. the counter-gradient vertical density flux occurs earlier.

In the shear dominated case the down-gradient fluxes are produced by the pumping of fluid through coherent hairpin-shaped vorticity. In the buoyancy dominated flow the counter-gradient fluid parcels induce helical vorticity structures as they move toward a position of neutral buoyancy.

1. Introduction

In both the atmosphere and the ocean, characterizing the small-scale turbulence is essential to understanding the vertical momentum and mass transport (Hopfinger 1987; Van Atta 1985). However, because the turbulence may be significantly altered by stable stratification, estimation of the vertical fluxes using only laboratory and field data may be very difficult. The accurate solution of the equations which govern stably stratified sheared turbulence is therefore an attractive approach to understanding such flows.

The general objective of this work was to investigate the effect of stable stratification on turbulent homogeneous shear flow by means of direct numerical simulation. Because such simulations are restricted to low Reynolds numbers the applicability of the numerical results to higher-Reynolds-number flows must be addressed. This was accomplished by comparing the simulation results to experimental data and by numerically studying the effect of Reynolds-number variation over the limited range accessible.

We begin with a brief description of previous related studies. In light of the volume of such work we only discuss those studies closely related to our own work.

1.1. *Previous studies*

Early analytical studies of homogeneous shear flow were conducted by von Kármán (1937). Several experimental studies followed, including the high-Reynolds-number passive scalar experiments of Tavoularis & Corrsin (1981) and the lower-Reynolds-number experiments of Rohr *et al.* (1988*a*). Both sets of experiments revealed an increase in the turbulent kinetic energy with increasing streamwise distance. The linearized analysis of Deissler (1961) revealed that the production of turbulent kinetic energy occurs at the largest lengthscales.

Recent direct simulations of homogeneous shear flow were performed by Rogers, Moin & Reynolds (1986). The instantaneous fields revealed the presence of coherent hairpin-shaped vorticity. These structures correspond to regions of intense turbulent kinetic energy production and vertical scalar flux. The hairpin structures found in the homogeneous flow (Rogers *et al.* 1986) resemble these found in regions far from the solid boundaries in the simulated turbulent channel flow of Moin & Kim (1985) and in the experimental visualization of a turbulent boundary layer by Head & Bandyopadhyay (1981). Robinson (1990) showed that contour surfaces of low pressure in the simulated boundary-layer results of Spalart (1988) also resembled one- and two-legged hairpins.

The behaviour of stably stratified turbulence without mean shear has been studied in several different experiments. The intuitive notion that the vertical velocity is suppressed by stable stratification was borne out by the experiments of Britter *et al.* (1983) and can be explained as a conversion of vertical kinetic energy into potential energy (Britter 1988).

The experiments of Stillinger, Helland & Van Atta (1983) showed that, at the onset of buoyancy effects, the scale of overturning motions (adapted from Ellison 1957) was approximately equal to the Ozmidov (1965) scale at which buoyancy forces are significant. As the flow evolved further the vertical density flux crossed zero, possibly indicating the presence of internal waves (Stewart 1969). In agreement with the predictions of Gibson (1980), Stillinger *et al.* (1983) showed that the lengthscales of active turbulence are confined between the decreasing Ozmidov scale and the increasing Kolmogorov scale.

Itwseire, Helland & Van Atta (1986) extended the experiments of Stillinger *et al.* (1983). They showed that the peak in the vertical density flux, which corresponds to the onset of buoyancy effects, occurs at the dimensionless time $Nt \approx 1.7$, where N is the Brunt–Väisälä (BV) frequency. At $Nt \approx 3$ the vertical density flux crosses zero, indicating that the turbulence is buoyancy dominated.

The air-flow experiments of Lienhard & Van Atta (1990) revealed a vertical heat flux reversal at larger scales coincident with the time, $Nt \approx 3$, at which the globally averaged flux became zero. However, the corresponding phase correlations did not support the existence of internal waves.

Gargett, Osborn & Nasmyth (1984) analysed field observations of stably stratified turbulence in the wake of a sill. They found that as the turbulence decayed the stratification induced anisotropy in the largest scales but the dissipation scales remained isotropic.

The first direct simulations of stably stratified turbulence were performed by Riley, Metcalfe & Weissman (1981). They observed oscillatory behaviour in the vertical kinetic energy and the potential energy. The exchange of energy between these two forms was explained in terms of the vertical density flux which oscillated about zero.

The first successful experiments of stably stratified homogeneous shear flow were performed by Rohr *et al.* (1988*b*). The Richardson number at which turbulence growth was suppressed was found to be 0.25 ± 0.05, in apparent agreement with the inviscid linear stability analysis of Taylor (see Miles 1961). In the cases which exhibited turbulence growth, both the overturning scale (Ellison 1957) and the Ozmidov scale grew, but their ratio approached a constant. When growth was suppressed the ratio of these scales approached the value found in the unsheared experiments of Stillinger *et al.* (1983).

The rapid distortion analysis of Hunt, Stretch & Britter (1988) showed that the temporal oscillations of the vertical velocity in the unsheared flow are damped in the presence of shear. Coincident with the vertical density flux reversal at $Nt = 2$ the Reynolds stress became counter-gradient (CG), i.e. there was a reversal in turbulence production.

In their simulations of randomly forced stably stratified turbulence, Herring & Métais (1989) found that the velocity field becomes nearly two-dimensional in agreement with the assertion of Riley *et al.* (1981), but the vertical variability of the horizontal layers controlled the dissipation rate. A weak inverse cascade of energy was also evident, a result consistent with the experimental results of Itsweire & Helland (1989).

The finite difference-spectral simulations of Gerz, Schumann & Elghobashi (1989) were the first numerical simulations of stably stratified sheared turbulence. They revealed the existence of a small-scale CG heat flux which was persistent in time at large Richardson number. According to the authors, the relatively small scalar dissipation rate at low Reynolds number and high Prandtl number sustains small-scale temperature fluctuations which become CG. The simulation results were also used to test the pressure–strain and pressure–temperature gradient closure models of Launder (1976), which were found to underestimate buoyancy effects at large Richardson number. In a related study, Gerz & Schumann (1989) varied the initial amount of potential energy over a relatively small range and found no significant differences in the flux development, aside from minor initial deviations.

1.2. *Research objectives*

The results of previous studies reveal issues which warrant further research and lead directly to the objectives of this investigation. First, the behaviour of the flow in terms of globally averaged statistics has not been thoroughly classified as a function of the Richardson number. Secondly, a systematic study of the effects of other dimensionless parameters is needed. These parameters include the Reynolds number, Schmidt (Prandtl) number, dimensionless shear rate (not discussed in this paper), and initial potential energy. Finally, the nature of the coherent structures at large Richardson number has not been completely determined. This structure must be known before its relationship to the transport processes can be established.

In the following section the governing equations and their numerical solution is described. The initial conditions used in the simulations are described in §3. The validation of the numerical method is then discussed in §4. This is followed by a discussion of the flow behaviour in terms of the Richardson number in §5. Section 6 contains a description of the effects of relevant parameters and is followed by a discussion of coherent structure in §7.

2. Mathematical considerations

2.1. *Fundamental equations*

The theoretical basis for this study is the conservation of mass equation for an incompressible fluid, the Boussinesq form of the Navier–Stokes equations, and a transport equation for the density:

$$U_{i,i} = 0, \tag{1}$$

$$U_{,t} + U_j U_{i,j} = -\frac{1}{\rho_0}\tilde{P}_{,i} - \frac{g}{\rho_0}\rho\delta_{i2} + \nu U_{i,jj}, \tag{2}$$

$$\varrho_{,t} + U_j \varrho_{,j} = \gamma \varrho_{,jj}, \tag{3}$$

where the density is expressed as

$$\varrho = \rho_0 + S_\rho x_2 + \rho \quad (\bar{\rho} = \rho_0 + S_\rho x_2), \tag{4}$$

and where ρ_0 is a constant reference density, $\bar{\rho}$ is the mean density, S_ρ is the specified mean density gradient, and ρ is the fluctuating density. The pressure is denoted by $\tilde{P}$ to signify that the hydrostatic pressure variation due to the mean density has been removed.

In the above equations the Einstein summation convention has been adopted and a comma denotes differentiation. This convention will be used interchangeably with the Cartesian system

$$U_i = (U_1, U_2, U_3) = (U, V, W), \tag{5}$$

$$x_j = (x_1, x_2, x_3) = (x, y, z). \tag{6}$$

2.2. *Solution procedure*

In this section we briefly describe the numerical method. For additional details see Holt (1990). As described by Batchelor (1953) and Townsend (1976) the statistical properties of homogeneous turbulence are invariant to translation, i.e. their spatial gradients are zero. Accordingly, the specified mean velocity and mean density gradients must be constant. The mean velocity, $\bar{U}_i$, is introduced by the change of variables

$$U_i = \bar{U}_i + u_i, \quad \bar{U}_i = (Sx_2, 0, 0), \tag{7}$$

where S is the shear rate and is the only non-zero element of the mean flow deformation tensor, $\bar{U}_{i,j}$, i.e. $S = \bar{U}_{1,2}$. The mean density, $\bar{\rho}$, was defined in (4) and, for future reference, a mean density gradient vector will be defined as $\bar{\rho}_{,j}$, with the only non-zero element being $S_\rho = \bar{\rho}_{,2}$. (The overbar defines a mean quantity which in these calculations refers to an ensemble average, not a volume average, over the solution domain.)

A homogeneous flow must be, in principle, unbounded. However, the numerical solution domain is finite and any boundary conditions selected will therefore be artificial. This requires that the simulation be monitored to ensure the solution is independent of the boundary conditions.

The simplest boundary condition is periodicity which also allows the use of highly accurate Fourier series representations of the fluctuating quantities. However, when the change of variables given by (4) and (7) are introduced into the governing equations (1)–(3), the mean flow quantities will produce spatially dependent coefficients and the solutions cannot satisfy periodic boundary conditions. This difficulty can be resolved by introducing a coordinate system that translates with the mean velocity (Rogallo 1981). The new coordinates will be denoted ξ_k; they are related to the stationary coordinates by

$$\xi_k = M_{kj} x_j, \tag{8}$$

$$\tau = t, \tag{9}$$

where the non-zero components of M_{kj} are $M_{11} = \beta_1$, $M_{22} = \beta_2$, $M_{33} = \beta_3$, and $M_{12} = -S\tau\beta_1$. The constants β_1, β_2, and β_3 are used to map the domain in x-space to a cubic box of length 2π in ξ-space.

Following the pseudo-spectral method (see Orszag 1969) of Rogallo (1981) the nonlinear terms are calculated in physical space. Transformations between physical and wave space are accomplished via the fast Fourier transform algorithm originally developed by Cooley & Tukey (1965).

The resulting ordinary differential equations are advanced in time using a second-order Runge–Kutta method. A second-order method was chosen to minimize storage requirements and to implement the random phase shift de-aliasing scheme of Rogallo (1981). Finally, the evolving solution consists of the Fourier coefficients of the fluctuating velocity, $\hat{u}_i$, and the fluctuating density, $\hat{\rho}$, in wave space $(\kappa_1, \kappa_2, \kappa_3)$.

2.3. *Transport equations*

The transport equation for the Reynolds stress (in physical space) may be obtained by standard methods (see Hinze 1975):

$$R_{ij,t} = P_{ij} - B_{ij} + T_{ij} - \epsilon_{ij}, \tag{10}$$

where

$$R_{ij} = \overline{u_i u_j}, \tag{11}$$

$$P_{ij} = -(\overline{u_j u_k}U_{i,k} + \overline{u_i u_k}U_{j,k}), \tag{12}$$

$$T_{ij} = \frac{1}{\rho_0}\overline{p(u_{i,j} + u_{j,i})} = \frac{1}{\rho_0}\overline{p s_{ij}}, \tag{13}$$

$$B_{ij} = \frac{g}{\rho_0}(\overline{u_i \rho}\delta_{j2} + \overline{u_j \rho}\delta_{i2}), \tag{14}$$

$$\epsilon_{ij} = 2\nu\overline{u_{i,k} u_{j,k}}. \tag{15}$$

In the above equations P_{ij} is the production due to the mean velocity field, T_{ij} is the redistribution due to pressure–strain interactions ($T_{ii} = 0$), B_{ij} represents the effect of buoyancy forces, and ϵ_{ij} is the dissipation due to viscous processes. In an analogous manner an equation for the turbulent density flux can be derived:

$$(\overline{\rho u_i})_{,t} = -(\overline{\rho u_k}U_{i,k} + \overline{u_i u_k \rho_{,k}}) - \frac{g}{\rho_0}\overline{\rho\rho}\delta_{i2} + \frac{1}{\rho_0}\overline{p\rho_{,i}} - \frac{1+Pr}{Pr}\nu\overline{\rho_{,k} u_{i,k}}, \tag{16}$$

where Pr is the Prandtl Number. For later reference the transport equations governing the non-zero R_{ij} and $\overline{\rho u_i}$ correlations are given below in Cartesian notation. First, we obtain the equation for the turbulent kinetic energy by taking the trace of (10):

$$\frac{\partial(\frac{1}{2}q^2)}{\partial t} = \mathcal{P} - \mathcal{B} - \epsilon, \tag{17}$$

where $q^2 = R_{ii}$ is twice the turbulent kinetic energy and

$$\mathscr{P} = -\overline{uv}S, \quad \mathscr{B} = \frac{g}{\rho_0}\overline{v\rho}, \quad \epsilon = \nu\overline{\frac{\partial u_i}{\partial x_k}\frac{\partial u_i}{\partial x_k}}. \tag{18}$$

An equation governing the turbulent density correlation may also be derived:

$$\frac{\partial(\frac{1}{2}\overline{\rho\rho})}{\partial t} = \mathscr{P}_\rho - \chi \tag{19}$$

where

$$\mathscr{P}_\rho = -\overline{v\rho}S_\rho, \quad \chi = \gamma\overline{\frac{\partial \rho}{\partial x_k}\frac{\partial \rho}{\partial x_k}}. \tag{20}$$

Finally, (10) and (16) in Cartesian notation are:

$$\frac{\partial\overline{uu}}{\partial t} = -2\overline{uv}S + \frac{1}{\rho_0}\overline{p\left(\frac{\partial u}{\partial x}+\frac{\partial u}{\partial x}\right)} - 2\nu\overline{\frac{\partial u}{\partial x_k}\frac{\partial u}{\partial x_k}}, \tag{21}$$

$$\frac{\partial\overline{vv}}{\partial t} = -2\frac{g}{\rho_0}\overline{v\rho} + \frac{1}{\rho_0}\overline{p\left(\frac{\partial v}{\partial y}+\frac{\partial v}{\partial y}\right)} - 2\nu\overline{\frac{\partial v}{\partial x_k}\frac{\partial v}{\partial x_k}}, \tag{22}$$

$$\frac{\partial\overline{ww}}{\partial t} = \frac{1}{\rho_0}\overline{p\left(\frac{\partial w}{\partial z}+\frac{\partial w}{\partial z}\right)} - 2\nu\overline{\frac{\partial w}{\partial x_k}\frac{\partial w}{\partial x_k}}, \tag{23}$$

$$\frac{\partial\overline{uv}}{\partial t} = -\overline{vv}S - \frac{g}{\rho_0}\overline{u\rho} + \frac{1}{\rho_0}\overline{p\left(\frac{\partial u}{\partial y}+\frac{\partial v}{\partial x}\right)} - 2\nu\overline{\frac{\partial u}{\partial x_k}\frac{\partial v}{\partial x_k}}, \tag{24}$$

$$\frac{\partial\overline{v\rho}}{\partial t} = -\overline{vv}S_\rho - \frac{g}{\rho_0}\overline{\rho\rho} + \frac{1}{\rho_0}\overline{p\left(\frac{\partial \rho}{\partial y}\right)} - \frac{1+Pr}{Pr}\nu\overline{\frac{\partial v}{\partial x_k}\frac{\partial \rho}{\partial x_k}}, \tag{25}$$

$$\frac{\partial\overline{u\rho}}{\partial t} = -\overline{uv}S_\rho - v\rho S + \frac{1}{\rho_0}\overline{p\left(\frac{\partial \rho}{\partial x}\right)} - \frac{1+Pr}{Pr}\nu\overline{\frac{\partial u}{\partial x_k}\frac{\partial \rho}{\partial x_k}}, \tag{26}$$

where the remaining correlations are zero by the spanwise symmetry imposed by the mean fields.

To end this section we note the following points. First, the deformation tensor of the velocity field, $U_{i,j}$, can be decomposed into the symmetric strain rate tensor, S_{ij}, and the anti-symmetric rotation rate tensor, Ω_{ij} (Townsend 1976). The mean flow deformation is decomposed as follows

$$\bar{S}_{ij} = \tfrac{1}{2}(\bar{U}_{i,j} + \bar{U}_{j,i}), \quad \bar{\Omega}_{ij} = \tfrac{1}{2}(\bar{U}_{i,j} - \bar{U}_{j,i}). \tag{27}$$

The strain rate is plane strain with expansive strain inclined at 45° from the horizontal and compressive strain at 135°. The rotation rate corresponds to solid-body rotation about the x_3-axis. Also, $2\mathscr{P} = P_{ii} = -2\overline{u_i u_k}\,\bar{U}_{i,k} = -2\overline{u_i u_k}\,\bar{S}_{ik}$ since the product of a symmetric tensor and an asymmetric tensor, $-2\overline{u_i u_k}\,\bar{\Omega}_{ik}$, is zero. Therefore, the turbulent kinetic energy is produced by the mean strain but not by the mean rotation (Rogers *et al.* 1986).

2.4. *Statistical quantities*

The numerical simulation results consist of the Fourier coefficients of the turbulent velocity and scalar fields. In this section these coefficients are related to the standard statistical measures which are used in this paper including lengthscales, two-point correlations, and energy spectra.

E_{ij} is termed the three-dimensional energy spectrum tensor. Since the velocities are real in physical space, the Fourier coefficients form a complex conjugate set. The three-dimensional energy spectrum tensor is also the Fourier transform of the two-point velocity correlation (Hinze 1975; Townsend 1976):

$$E_{ij}(\kappa_n) = \frac{1}{(2\pi)^3}\int Q_{ij}(r_l)\exp^{(-\iota\kappa_n r_l)}\,\mathrm{d}r_l \tag{28}$$

where Q_{ij}, the three-dimensional two-point correlation, is defined as

$$Q_{ij}(r_l) = \overline{u_i(x_m)\,u_j(x_m+r_l)}. \tag{29}$$

In homogeneous turbulence Q_{ij} is only a function of separation distance, r_l, since statistical quantities are independent of position, x_m. The two-point correlation is also symmetric, therefore $E_{ij} = E_{ji}$.

Spectral statistics may be derived from E_{ij} by summing over selected wavenumbers. The one-dimensional energy spectrum in the κ_α ($\alpha = 1, 2$, or 3) direction is

$$E_{ij}(\kappa_\alpha) = \int E_{ij}(\kappa_\alpha, \kappa_\beta, \kappa_\gamma)\,\mathrm{d}\kappa_\beta\,\mathrm{d}\kappa_\gamma \quad (\alpha \neq \beta \neq \gamma). \tag{30}$$

By integrating over spherical shells the radial energy spectrum is obtained

$$E_{ij}(\kappa) = \int E_{ij}[\kappa, A(\kappa)]\,\delta A(\kappa). \tag{31}$$

The one-dimensional two-point correlation is

$$Q_{ij}(r_\alpha) = \int Q_{ij}(r_\alpha, r_\beta, r_\gamma)\,\mathrm{d}r_\beta\,\mathrm{d}r_\gamma \quad (\alpha \neq \beta \neq \gamma). \tag{32}$$

This leads to the definition of the integral scale

$$\Lambda_{ij;\alpha} = \frac{1}{R_{ij}}\int Q_{ij}(r_\alpha)\,\mathrm{d}r_\alpha. \tag{33}$$

Finally, the Taylor microscales are defined by

$$\lambda_{ij;\alpha} = \frac{u_i'}{u_{j,\alpha}'}, \tag{34}$$

where primes denote r.m.s. quantities. For example, $u_{1,2}' = (\overline{u_{1,2}u_{1,2}})^{\frac{1}{2}}$.

3. Initial conditions

To ensure accurate resolution of all relevant scales of motion and to enable the simulations to be extended to large dimensionless times the initial conditions need to be carefully designed.

The initialization algorithm in this and other direct simulation methods (Gerz *et al.* 1989; Riley *et al.* 1981) produces the specified initial radial energy spectrum $E = \frac{1}{2}E_{ii}(\kappa)$ and satisfies the conservation of mass equation but does not yield nonlinear spectral transfer of energy. Zero transfer initial conditions are acceptable provided the ratio of the turbulence and mean flow timescales, $S^* = Sq^2/\epsilon$, is sufficiently small (see also Rogallo 1981; Rogers *et al.* 1986). In other words, the mean shear must not dominate the turbulence and prevent nonlinear interactions from

Ri variation simulations (*h* series)

N_x, N_y, N_z	128, 128, 128
$\beta_1, \beta_2, \beta_3$	$2^{-\frac{2}{3}}, 2^{\frac{1}{3}}, 2^{\frac{1}{3}}$
S, ν, g, ρ_0	$20\sqrt{2}, 0.01, 980.665, 1.006$
$\kappa_0, \kappa_c, e, e_\rho, Re_\lambda, Re_A$	16, 32, 1, 0, 52, 57

Run designation	*Ri*
ge	0.0
hb	0.058
hd	0.088
hc	0.113
hf	0.25
he	0.5
hg	1.0

TABLE 1. Simulations in which the Richardson number was varied, denoted as the *h* series simulations

Re_0 variation simulations (*x* and *y* series)

N_x, N_y, N_z	128, 128, 128
$\beta_1, \beta_2, \beta_3$	$2^{-\frac{2}{3}}, 2^{\frac{1}{3}}, 2^{\frac{1}{3}}$
Sc, g, ρ_0	1.0, 980.665, 1.006

Run designation	*Ri*	S, ν	$\kappa_0, \kappa_c, e, e_\rho, Re_\lambda, Re_A$
la	0.058	$40\sqrt{2}, 0.02$	16, 32, 1, 0, 26, 29
xb	0.113	$10\sqrt{2}, 0.005$	16, 32, 1, 0, 104, 115
xc	0.5	$10\sqrt{2}, 0.005$	16, 32, 1, 0, 104, 115
ya	0.15	$10\sqrt{2}, 0.005$	$4, 40, 0.\bar{4}, 0, 104, 155$
yb	0.5	$10\sqrt{2}, 0.005$	$4, 40, 0.\bar{4}, 0, 104, 155$
yd	1.0	$10\sqrt{2}, 0.005$	$4, 40, 0.\bar{4}, 0, 104, 155$

TABLE 2. Simulations in which the initial Reynolds number was varied, denoted as the *x* series and *y* series simulations

Sc variation simulations (*p* series)

N_x, N_y, N_z	128, 128, 128
$\beta_1, \beta_2, \beta_3$	$2^{-\frac{2}{3}}, 2^{\frac{1}{3}}, 2^{\frac{1}{3}}$
S, ν, g, ρ_0	$20\sqrt{2}, 0.01, 1.0, 980.665, 1.006$
$\kappa_0, \kappa_c, e, e_\rho, Re_\lambda, Re_A$	16, 32, 1, 0, 52, 57

Run designation	*Ri*	*Sc*
pd	0.088	2
pl	0.5	0.1
pm	0.5	0.5
pe	0.5	2
pg	0.5	4

TABLE 3. Simulations in which the Schmidt number was varied, denoted as the *p* series simulations

η_0 variation simulation (e series)

N_x, N_y, N_z		128, 128, 128	
$\beta_1, \beta_2, \beta_3$		$2^{-\frac{2}{3}}, 2^{\frac{1}{3}}, 2^{\frac{1}{3}}$	
S, ν, Sc, g, ρ_0		$20\sqrt{2}, 0.01, 1.0, 980.665, 1.006$	
Run designation	Ri	$\kappa_0, \kappa_c, e, e_\rho, Re_\lambda, Re_\Lambda$	η_0
ec	0.088	$16, 32, 1, 4.91 \times 10^{-5}, 52, 57$	2
ea	0.5	$16, 32, 1, 1.40 \times 10^{-4}, 52, 57$	1
ed	0.5	$16, 32, 1, 9.82 \times 10^{-4}, 52, 57$	7

TABLE 4. Simulations in which the initial ratio of potential to vertical kinetic energy was varied, denoted as the e series simulations

Simulations of Rohr's (1985) experiments (r series)

N_x, N_y, N_z		128, 128, 128
$\beta_1, \beta_2, \beta_3$		$\frac{1}{8}, \frac{1}{4}, \frac{1}{4}$
S, ν, Sc, g, ρ_0		$1.13, 0.01, 2.0, 980.665, 1.006$
Run designation	Ri	$\kappa_0, \kappa_c, e, e_\rho, Re_\lambda, Re_\Lambda$
ra	0	$0.25, 9.0, 0.303, 0, 99, 212$
rb	0.075	$0.25, 10.0, 0.272, 5.55 \times 10^{-10}, 92, 195$
rc	0.21	$0.25, 11.0, 0.2465, 2.09 \times 10^{-9}, 87, 183$
rd	0.37	$0.25, 11.0, 0.2465, 3.91 \times 10^{-9}, 87, 183$
re	1.0	$0.25, 11.0, 0.2465, 3.91 \times 10^{-9}, 87, 193$

TABLE 5. Simulations that replicate the experiments of Rohr (1985), denoted as the r series simulations

developing. In the low shear rate simulations reported in this paper the dimensionless shear rate, S^*, was initially approximately 5 and increased in time to approximately 11. This asymptotic value agrees with the experimental data of Tavoularis & Corrsin (1981) and Rohr (1985).

For low shear rate simulations pulse initial spectra are also acceptable, and the calculations are initiated by specifying the energy spectra as follows

$$E(\kappa) = e \quad (\kappa_0 \leqslant \kappa \leqslant \kappa_c), \tag{35}$$

$$E(\kappa) = 0 \quad (\kappa < \kappa_0, \quad \kappa > \kappa_c), \tag{36}$$

and by assuming the initial potential energy is zero (see §6.2). In (35) and (36) e is a constant, and κ_0 and κ_c define the width of the pulse. Zero initial energy was specified in the range $\kappa < \kappa_0$ to accommodate large-scale growth.

The simulation parameters (in cgs units) are summarized in tables 1–4. Each table summarizes the simulations designed to investigate the effects of varying one of the following parameters: Ri, Re, Sc, and $\eta = PE/VKE$ (see following text for definitions). For completeness, we have also listed the initial conditions used to simulate the experiments of Rohr (1985) in table 5. In these tables N_x, N_y, and N_z are the numbers of grid points, and β_1, β_2, and β_3 are coordinate stretching factors. The computational domain was longer in the streamwise direction, i.e. $\beta_1 < \beta_2 = \beta_3$ to allow for shear-induced growth of the integral scales. The column headings κ_0, κ_c, e, and e_ρ, refer to the pulse initial spectra for $\frac{1}{2}q^2$ and $\frac{1}{2}\overline{\rho\rho}$. (The initial velocity and density fields were uncorrelated.) The initial Reynolds numbers $Re_\lambda = q\lambda_{11;1}/\nu$ and $Re_\Lambda = q\Lambda_{11;1}/\nu$ are also listed.

4. Validation of the numerical method

Before proceeding with the numerical investigation of stably stratified shear flow, a series of simulations was performed to validate the numerical method. Preliminary validation studies including reproducing some of the unstratified shear flow simulations of Rogers *et al.* (1986), the stratified unsheared simulations of Riley *et al.* (1981), and the stratified shear flow simulations of Gerz *et al.* (1989). The results of these comparisons indicate that the present numerical method performs satisfactorily (see Holt 1990).

The final validation study was a direct simulation of the experiments of Rohr (1985), see also Rohr *et al.* (1988*b*). These results will be presented in detail to introduce the effects of Richardson-number variation.

Comparison between the simulated and experimental results will be shown for Richardson numbers, Ri, of 0, 0.075, 0.21, and 0.37 (based on initial conditions) with additional simulation results at $Ri = 1.0$. The Richardson number is defined as

$$Ri = \frac{N^2}{S^2} = \frac{(g/\rho_0)S_\rho}{S^2} \tag{37}$$

where N is the Brunt–Väisälä frequency.

The experimental data nearest the grid were reported at a dimensionless time $St \approx 1.2$. This required that isotropic initial conditions ($St = 0$) be specified in the simulations and allowed to develop to $St = 1.2$ so as to achieve agreement with the measured u', v', ρ', and ϵ. Comparison between the physical experiments, which vary in space, and the numerical simulations, which vary in time, were effected by a Galilean transformation of the numerical data using the mean velocity ($x = \bar{U}t$).

Figure 1 presents the r.m.s. streamwise velocity fluctuations, u', as a function of dimensionless time, St. At $Ri = 0$, u' increases with time (after an initial decay) owing to the production term $-2\overline{uv}S$ in (21). This may be explained by considering a positive vertical velocity fluctuation ($v > 0$) which moves a parcel of slow fluid ($u < 0$) upward into faster fluid, resulting in $uv < 0$ and a positive production term. (Production also results from the downward movement of faster fluid; essentially this is the basis of Prandtl's mixing length model.) As Ri increases the growth rate of u' decreases owing to the suppression of production, as discussed below. The agreement between the numerical and experimental results for $St < 6$ is only fairly good. The discrepancy is partly due to grid-induced anisotropy in the experiment which resulted in $u' > v'$ initially. In addition, the experiments exhibit quasi-isotropic decay for longer times than the simulations.

The vertical velocity development is shown in figure 2. At $Ri = 0$, v' increases even though there is no production term in (22). In this case energy is transferred from u' to v' through pressure–strain redistribution. (The behaviour of the pressure–strain and pressure–density gradient terms in (21)–(26) are reported in Holt 1990.) The growth of v' is reduced with increasing Ri for two reasons. First, with the decrease in u', less energy is transferred to v'. Secondly, the stable stratification, through the term $-2(g/\rho_0)\overline{v\rho}$ in (22), limits the growth of v'. As explained above, a positive vertical velocity fluctuation lifts slow fluid into faster ambient fluid. The slow fluid also originates in a region of heavy fluid ($\rho > 0$) which is lifted ($v > 0$) into lighter fluid, resulting in $v\rho > 0$. Thus the term $-2(g/\rho_0)\overline{v\rho}$ in (22) acts to decrease v'. The correlation $\overline{v\rho}$ also appears in the term $-\overline{v\rho}S_\rho$ in (19) where it causes ρ' to increase. Physically, vertical kinetic energy ($VKE = \frac{1}{2}\overline{vv}$) is converted into potential energy

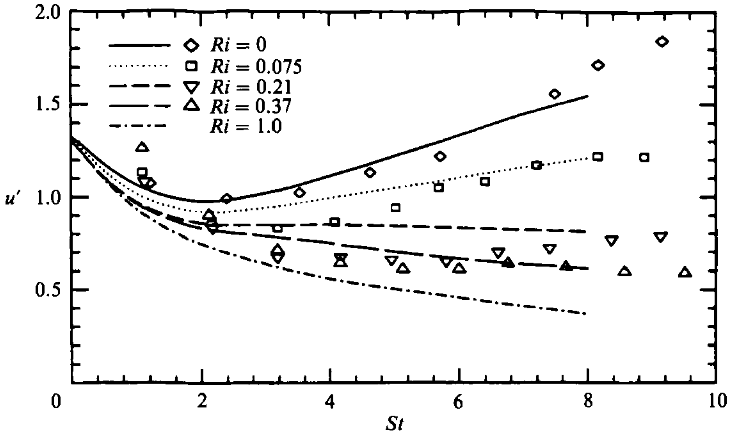

FIGURE 1. Evolution of the simulated and experimental streamwise velocities. Symbols refer to the experiments of Rohr (1985).

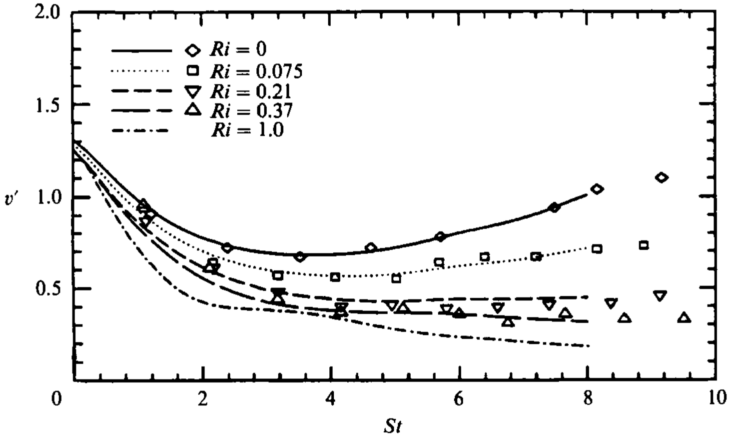

FIGURE 2. Evolution of the simulated and experimental vertical velocities. Symbols refer to the experiments of Rohr (1985).

$(PE = (-g/\rho_0)(\tfrac{1}{2}\overline{\rho\rho})/S_\rho)$ as heavy parcels of fluid are lifted upward. (The downward motion of light fluid is equally likely.)

The increase in ρ' with increasing Ri is shown in figure 3. As Ri increases a given v induces a larger ρ since S_ρ increases. At $Ri = 1.0$ and small St the *VKE* generates significant *PE*. However, the *PE* later decreases as it is converted back to *VKE*; this is discussed below. A maximum Schmidt number ($Sc = \nu/\gamma$) of 2 could be specified in the simulations while maintaining resolution of the scalar dissipation scales. However, in the experiments $Sc \approx 700$. Despite the differences in Péclet number ($Pe = ScRe$) between the experimental and numerical flows, differences between the experimental and simulated values of ρ' which are evident at small St, tend to vanish at large St. This apparent Péclet-number independence suggests that at the larger values of St in figure 3 the flow is being controlled by large-scale motion. However, at even larger values of St for the high Ri flows, when dissipation becomes important, the results should depend strongly on Péclet number.

The development of the normalized vertical density flux, $v\rho/v'\rho'$, is shown in figure 4. Since slow fluid is correlated with heavy fluid and fast fluid is correlated with

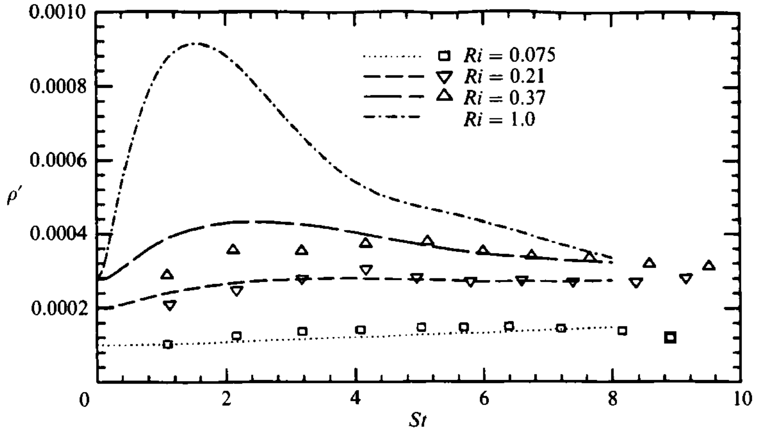

FIGURE 3. Evolution of the simulated and experimental densities. Symbols refer to the experiments of Rohr (1985).

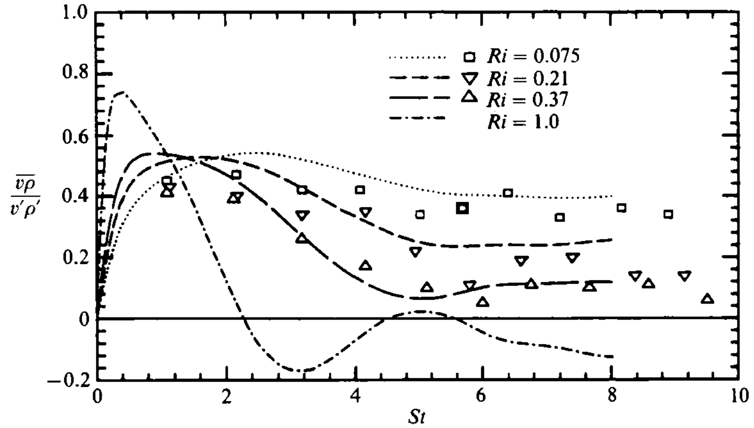

FIGURE 4. Evolution of the simulated and experimental vertical density fluxes. Symbols refer to the experiments of Rohr (1985).

light fluid ($-\overline{u\rho} > 0$), the behaviour of the normalized Reynolds stress, $-\overline{uv}/u'v'$, is similar to that of $\overline{v\rho}/v'\rho'$ (see also §5.2). Figure 4 shows that for $Ri < 1.0$, $\overline{v\rho} > 0$ (and $-\overline{uv} > 0$). As explained above these down-gradient (DG) fluxes result from the upward movement of slow, heavy fluid into faster, lighter ambient fluid or the downward movement of fast, light fluid into slower, heavier ambient fluid. The DG fluxes produce turbulent kinetic energy and scalar fluctuations (see (17) and (19)). However, the normalized DG fluxes decrease with increasing Ri. This is explained as follows. First, the decrease in v' with increasing Ri suppresses turbulence production, $\mathscr{P} = -\overline{uv}S$, through the term $-\overline{vv}S$ in (24). Secondly, as reflected in the term $-(g/\rho_0)\overline{u\rho}$ in (24), the vertical transport of momentum ($-\overline{uv} > 0$) also results in heavy fluid parcels being lifted against gravity, (gain of *PE* at expense of *VKE*) further weakening the production. Similarly, in the transport equation for $\overline{v\rho}$ (25) the increase in *PE* (the term $-(g/\rho_0)\overline{\rho\rho}$) occurs at the expense of *VKE* (the term $-\overline{vv}S_\rho$). This energy conversion limits $\overline{v\rho}$ and, therefore, the production of scalar fluctuations.

At $Ri = 1.0$ the vertical density flux reverses sign, becoming counter-gradient (CG). (We define the flux to be CG when it occurs against the mean density gradient.)

The CG vertical density flux can be interpreted as a return of *PE* to *VKE* as heavy fluid parcels ($\rho > 0$) descend ($v < 0$) toward their neutrally buoyant positions (or as light fluid parcels ascend). This interpretation is valid provided the heavy fluid does not diffuse its density difference to its environment before descending, i.e. *Sc* must be sufficiently large. The descent of heavy fluid implies a descent of slow fluid ($-\overline{u\rho} > 0$) so that a CG vertical density flux ($\overline{v\rho} < 0$) typically results in a CG momentum flux ($-\overline{uv} < 0$) and negative turbulence production. The decay of u' at large *Ri* is thereby enhanced.

5. Richardson number classification

We turn now to the first stated objective of this paper, to describe the physics of stably stratified shear flow in terms of the primary dimensionless parameter, the Richardson number. Unless otherwise stated the results are obtained from the *h* series simulations which are summarized in table 1.

5.1. *The stationary Richardson number*

In §4 we showed that the growth rates of u' and v' decrease with increasing *Ri*. In the present section we investigate this observation further. The temporal development of q^2 is determined by production ($\mathscr{P}$), buoyancy forces ($\mathscr{B}$), and dissipation (ϵ) as shown in (17). We define the dimensionless growth rate parameter

$$F = \frac{\mathscr{P} - \mathscr{B}}{\epsilon} \tag{38}$$

to represent the relative importance of these terms. The dimensionless growth rate of q^2 is then determined by

$$\frac{1}{\epsilon}\frac{\partial \frac{1}{2}q^2}{\partial t} = F - 1. \tag{39}$$

As shown in figure 5(*a*), $F > 1$ for small *Ri* and q^2 grows, whereas at large *Ri*, $F < 1$ and q^2 decays. This suggests that there is a stationary Richardson number, Ri_s, at which $F \approx 1$ and q^2 is approximately constant in time. For the *h* series simulations shown in figure 5(*a*), $Ri_s = 0.088$. Reported values of Ri_s vary, from approximately 0.21 in the experiments of Rohr (1985) to 0.1 in the simulations of Gerz *et al.* (1989). In our simulations Ri_s varied from 0.058 to 0.21.

The following dimensional analysis of the equation for q^2 (equation (17)) shows that Ri_s depends upon three parameters. Let L, L_ρ, q_c, and ρ_c be characteristic length and intensity scales for the velocity and scalar fields. The dimensionless form of (17) is then

$$\frac{\partial \frac{1}{2}q^{*2}}{\partial t^*} = -\overline{u^*v^*}S - \overline{v^*\rho^*}Ri\frac{1}{\mathscr{L}}\mathscr{S} - \frac{1}{\mathscr{R}}\overline{\frac{\partial u_i^*}{\partial x_k^*}\frac{\partial u_i^*}{\partial x_k^*}}, \tag{40}$$

where

$$\mathscr{L} = \frac{-S_\rho/\rho_c}{S/q_c}, \quad \mathscr{S} = SL/q_c, \quad \mathscr{R} = q_cL/\nu. \tag{41}$$

In the above expressions $\mathscr{L}$ is the ratio of the lengthscales of the velocity and scalar fields. The parameter $\mathscr{S}$ is a dimensionless shear rate, L/q_c being a turbulence timescale. (If L is chosen to be q^3/ϵ then $\mathscr{S} = S^*$.) Finally, $\mathscr{R}$ is a Reynolds number.

The relevance of these three parameters to the stationary condition may be seen

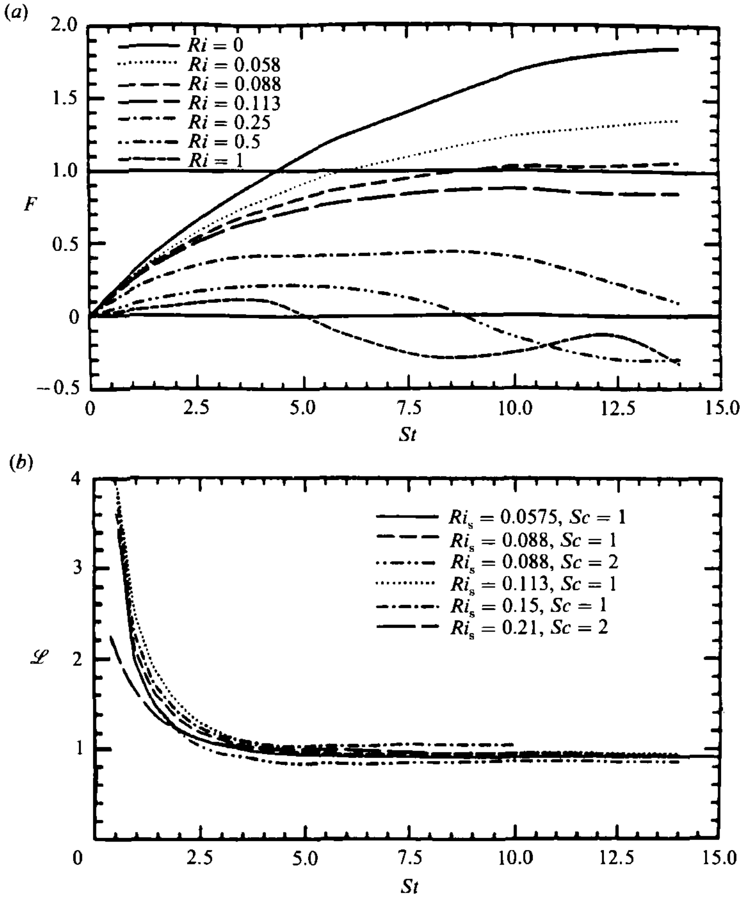

FIGURE 5. (*a*) Evolution of the growth rate parameter as a function of Richardson number. (*b*) Evolution of the lengthscale ratio at Ri_s.

by considering the fact that at $Ri = Ri_s$ the dimensionless growth rate is zero. Equation (40) then indicates that

$$Ri_s = f(\mathscr{L}, \mathscr{S}, \mathscr{R}). \tag{42}$$

Rogers *et al.* (1986) and Shirani, Ferziger & Reynolds (1981) both found a weak dependence of $\mathscr{L}$ upon the Prandtl number at $Ri = 0$. Thus, L_p is proportional to L, which means that the lengthscales of the scalar field are controlled by the velocity field. This implies that Ri_s may be only weakly dependent upon $\mathscr{L}$ and therefore the Prandtl (or Schmidt) number, a result which is confirmed in figure 5(*b*) (see §6.2).

Now consider the case of low shear rate found in both the experiments of Rohr (1985) and the present simulations. For a given $\mathscr{S}$, (42) suggests that Ri_s depends upon $\mathscr{R}$. The simulation results presented in figure 6 illustrate that Ri_s increases with increasing integral scale Reynolds number, $Re_{\Lambda_{11;1}} = q\Lambda_{11;1}/\nu$ (where the Reynolds number is defined based on final lengthscales). This is because as $Re_{\Lambda_{11;1}}$ increases, the separation between the largest lengthscales and the smallest lengthscales increases and viscous effects become less important in controlling the growth of q^2. Increased stratification (larger Ri_s) is therefore required to suppress $\mathscr{P}$ and control the growth of q^2.

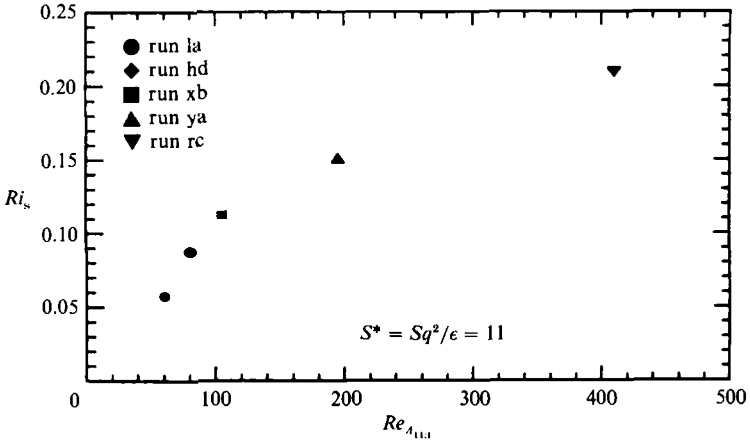

FIGURE 6. Stationary Richardson number as a function of the integral scale Reynolds number.

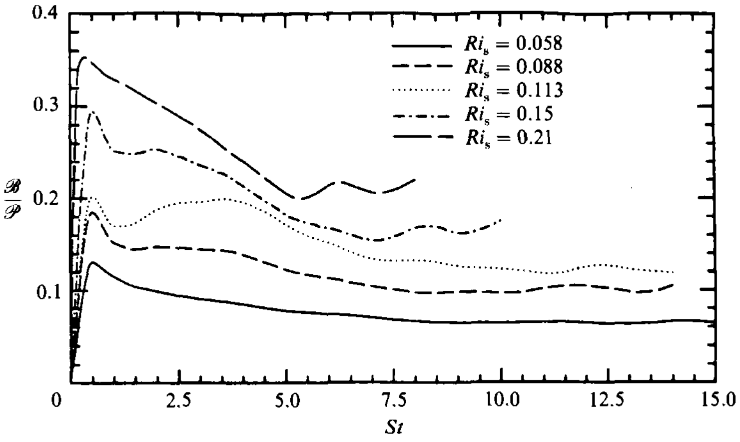

FIGURE 7. Evolution of the ratio of buoyancy and production at Ri_s.

The parameter F can also be written

$$F = \frac{\mathscr{P}}{\epsilon}\left(1 - \frac{\mathscr{B}}{\mathscr{P}}\right). \tag{43}$$

Consistent with the argument made above, as $Re_{A_{11:1}}$ increases, $\mathscr{P}/\epsilon$ increases and a larger $\mathscr{B}/\mathscr{P}$ is required to maintain $F \approx 1$. Indeed, at Ri_s the ratio $\mathscr{B}/\mathscr{P}$ increases from approximately 0.07 to 0.22 with increasing $Re_{A_{11:1}}$ (see figure 7). The buoyancy term is, therefore, a relatively small part of the energy budget at the stationary condition. Thus, stratification does not directly reduce the growth of q^2 (i.e. is not a kinetic energy sink). Rather, $F \approx \mathscr{P}/\epsilon$ and the role of stratification is indirect via the suppression of $\mathscr{P}$. This can be seen by examining (21)–(26) which show the complex interaction between the various buoyancy and shear (turbulence production) terms in the transport equations.

At large Reynolds number Ri_s seems to approach the *critical* Richardson number (0.25) predicted by the inviscid linear stability analysis of Taylor (see Miles 1961). This is interesting but will not be pursued in detail since the assumptions of the analysis (inviscid linearity) are not satisfied in the simulations. As will be discussed below, a finite dissipation rate is necessary for maintaining stationarity. Also,

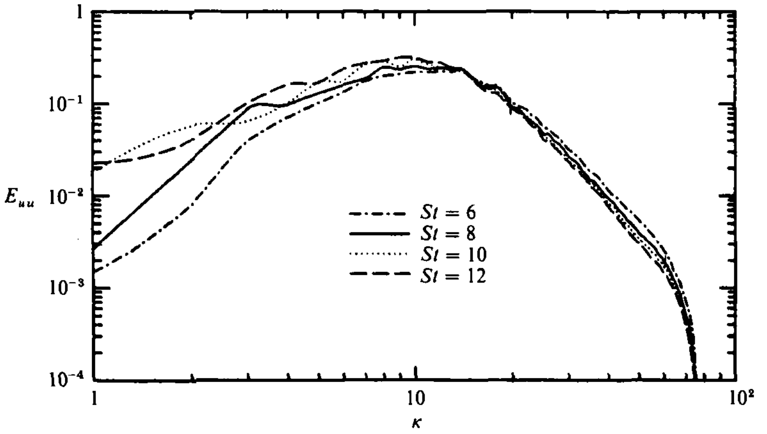

FIGURE 8. Evolution of the radial spectra of the streamwise energy at $Ri_s = 0.088$.

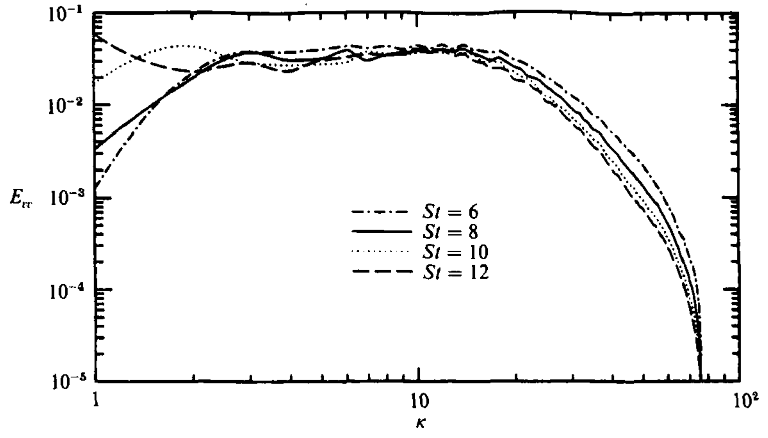

FIGURE 9. Evolution of the radial spectra of the vertical energy at $Ri_s = 0.088$.

significant nonlinearity is present in the simulations. The degree of nonlinearity may be measured by the ratio $S\lambda/q$ where $\lambda = (5q^2\nu/\epsilon)^{\frac{1}{2}} \sim \lambda_{ik;j}$. (Other measures of linearity are S^* and $SA_{11;1}/q$.) If $S\lambda/q \gg 1$ the mean shear–turbulence interactions dominate the nonlinear turbulence–turbulence interactions. However, in the simulations $S\lambda/q \approx 1.4$.

We remark that at a large dimensionless shear rate the effects of viscosity and nonlinear interactions are minimal, see Holt (1990). This precludes the identification of a stationary Richardson number. Instead, one can only identify a sufficient condition for lack of growth in q^2.

At $Ri = Ri_s$, q^2 is nearly constant in time. However, the radial energy spectra, $E(\kappa) = \frac{1}{2}E_{ii}(\kappa)$, at Ri_s reveal that the lowest wavenumber modes gain energy while the highest wavenumber modes lose energy so that the spectra are not stationary. Energy spectra at $Ri_s = 0.088$ will be presented to demonstrate this point. First, E_{ii} is dominated by the streamwise velocity ($\overline{uu}/q^2 \approx 0.63$). Thus, the spectra E_{uu} shown in figure 8 illustrate the spectral evolution at Ri_s. The spanwise velocity spectra ($\overline{ww}/q^2 \approx 0.25$) behave similarly. The low-wavenumber modes of the vertical velocity spectra ($\overline{vv}/q^2 \approx 0.12$) are, however, more stationary in time (figure 9). The scalar

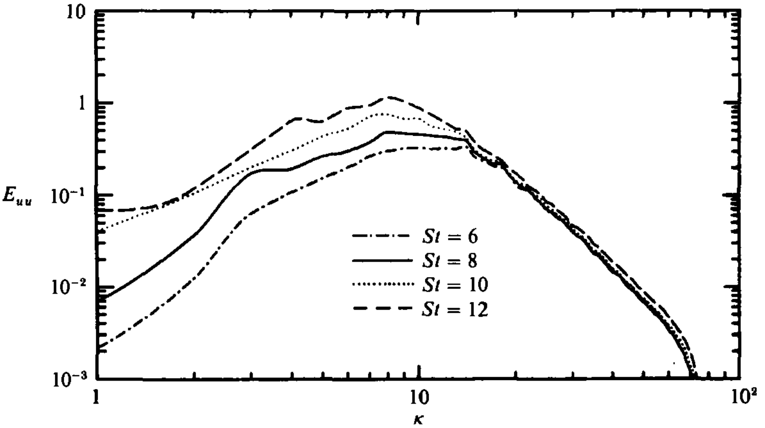

FIGURE 10. Evolution of the radial spectra of the streamwise energy at $Ri = 0$.

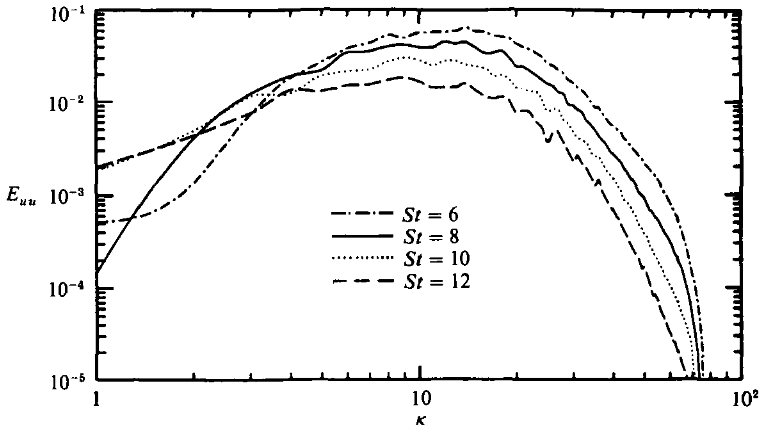

FIGURE 11. Evolution of the radial spectra of the streamwise energy at $Ri = 0.5$.

spectrum, $E_{\rho\rho}$, evolves similarly to E_{uu}, as the scalar dynamics are driven by the velocity field. In contrast to the spectral behaviour at Ri_s, at $Ri = 0$ all scales gain energy and the spectra become more broad banded (see figure 10) while at $Ri = 0.5$ almost all scales lose energy (figure 11).

The spectral evolution can be explained physically as follows. At $Ri = 0$ significant production of turbulent kinetic energy occurs in the most energetic modes. Some of this energy is then transferred to higher wavenumbers. At $Ri = Ri_s$ the production is reduced and less energy is transferred. Consequently, dissipation processes dominate at the higher wavenumbers and these scales lose energy. This physical picture applies directly to E_{uu} as the production appears in the equation governing $\overline{uu}$, whereas the pressure–strain redistribution of energy results in a similar evolution of E_{vv} and E_{ww}.

The physical interpretation of the spectral evolution assumes that production and spectral energy transfer are reduced at Ri_s. At $Ri = 0$ the radial co-spectrum E_{uv} shows that production ($\mathscr{P} = \overline{uv}S$) increases in time at the most energetic wavenumbers (see figure 12). At Ri_s, $\mathscr{P}$ is indeed weaker since the co-spectra are now stationary at the most energetic wavenumbers and decreasing at larger wavenumbers (see figure 13, also note scale change from figure 12).

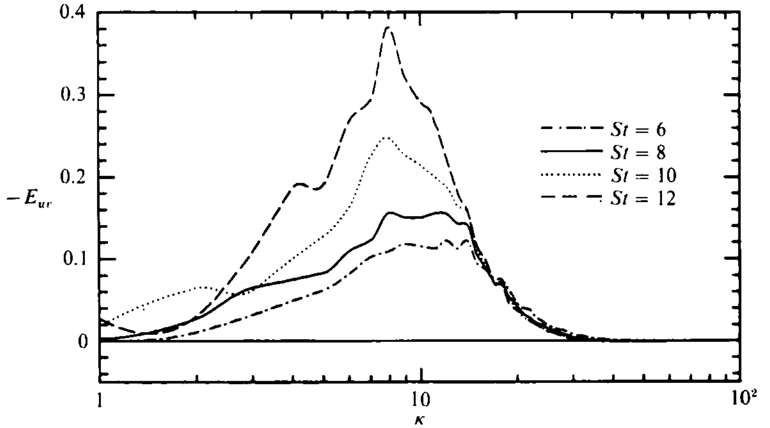

FIGURE 12. Evolution of the radial co-spectra of the Reynolds stress at $Ri = 0$.

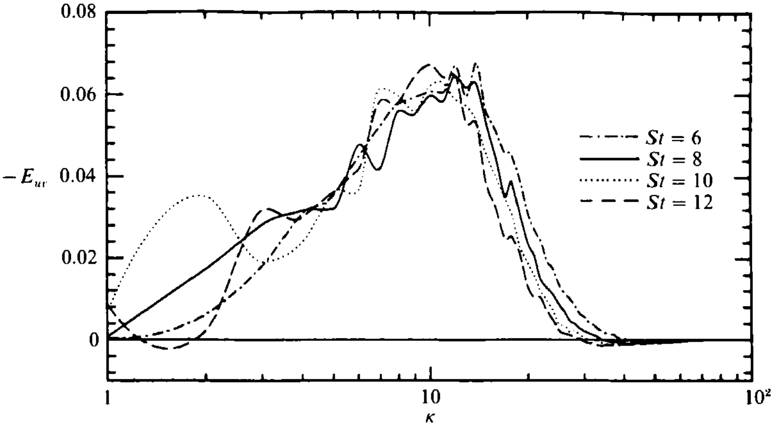

FIGURE 13. Evolution of the radial co-spectra of the Reynolds stress at $Ri_s = 0.088$.

To examine the nonlinear energy transfer we present the radial transfer spectra of the streamwise energy, N_{uu}, in figure 14. (N_{uu} is part of the tensor, N_{ij}, representing the nonlinear transfer of energy between wavenumber components of the energy spectrum. In isotropic turbulence, for example, all components of N_{ij} are negative at low wavenumbers and positive at high wavenumbers because the energetic large scales transfer energy to the smaller scales.) The transfer spectra have been normalized by the Kolmogorov velocity, $V_k = (\epsilon\nu)^{\frac{1}{4}}$, to facilitate comparison over a range of Ri. From figure 14 it is clear that stratification reduces spectral transfer as assumed above. That is, the transfer from the energetic large scales to the smaller scale motions is reduced. The transfer spectra are also shifted to larger wavenumbers at $Ri = Ri_s$. This may be due to the suppression of production at the lower wavenumbers as explained previously. Furthermore, the near two-dimensionality of the velocity field $(\overline{uu}/q^2 + \overline{ww}/q^2 \approx 0.88)$ implies reduced transfer, presumably through reduced vortex stretching. However, figure 14 does not exhibit the characteristic inverse energy cascade of strictly two-dimensional (unsheared) turbulence (see Itsweire & Helland 1989). An explanation as to why the flow does not exhibit the characteristics of two-dimensional turbulence has been proposed by Métais & Herring (1989). They suggest that at large Ri the flow is mainly in

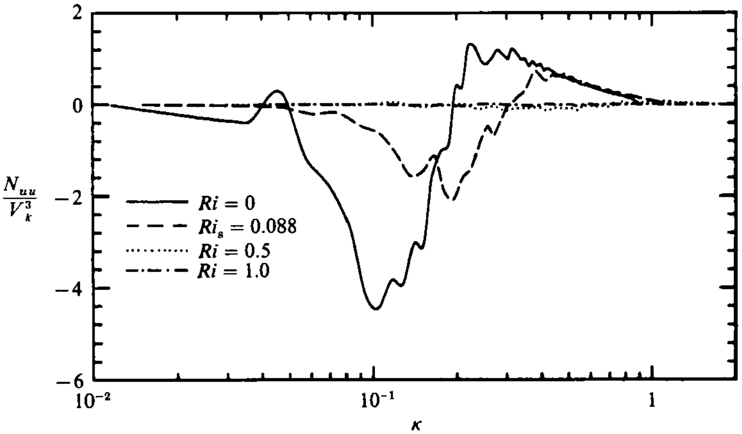

FIGURE 14. Radial spectra showing transfer of streamwise energy at $St = 12$.

horizontal layers, but unlike pure two-dimensional turbulence the vertical variability of the turbulence is important. This implies that horizontal vorticity and small-scale energy may be generated by vertical shear due to friction between the layers.

An alternative way of describing the effects of stratification on energy transfer (see, for example, Gerz & Schumann 1991) is that with stable stratification the largest, energy-containing, eddies do not grow as much as they would in the absence of buoyancy. The spectral transfer of energy is not done at the largest scales but rather by eddies which are not yet influenced by buoyancy. This viewpoint originates from the idea that turbulent scales are only influenced by buoyancy when their scale is about equal to the Ozmidov scale. It does not, however, explain why all scales of motion are affected by buoyancy at large Ri (see figure 11, for example), an effect which is accounted for by examining the influence of stratification on the production process itself. We close this section with two additional comments. First, the Kolmogorov scaled energy spectra, $E_{\alpha\alpha}(L_k \kappa)/V_k^2 L_k$ where $L_k = (\nu^3/\epsilon)^{\frac{1}{4}}$, exhibit small-scale collapse as expected. Secondly, since the stratified shear flow is anisotropic it is of interest to inspect the one-dimensional spectra, $E_{ij}(\kappa_l)$. The behaviour of these one-dimensional spectra is consistent with the radial spectra at all simulated Ri. (See Holt (1990) for a discussion of these points.)

5.2. *The transition Richardson number*

Although Ri_s marks the boundary between growth and decay of q^2, counter-gradient (CG) fluxes are found only at much larger Ri. This is illustrated in figure 15 which shows the evolution of the normalized vertical density flux $\overline{v\rho}/v'\rho'$. At $Ri_s = 0.088$ the normalized flux evolves in much the same way as the passive scalar case. The CG flux appears only at $Ri = 0.5$ and 1.0. In these cases $\overline{v\rho}/v'\rho'$ evolves very differently, exhibiting oscillations which modulate the small negative mean correlations.

The differences in the temporal development of $\overline{v\rho}/v'\rho'$ allow us to partition the results into two regimes separated by $Ri = 0.25$, at which $\overline{v\rho}/v'\rho'$ approaches zero for large St. The normalized Reynolds stress, $-\overline{uv}/u'v'$, behaves similarly (see figure 16) since slow fluid is correlated with heavy fluid and fast fluid is correlated with light fluid, i.e. $-\overline{u\rho}/u'\rho' \approx 0.7$ as shown in figure 17. Hence, $-\overline{uv}/u'v' \rightarrow 0$ at $Ri = 0.25$. On the basis of these observations we define the transition Richardson number, Ri_t, as the Richardson number at which the fluxes $\overline{v\rho}/v'\rho'$ and $\overline{uv}/u'v'$ approach zero at

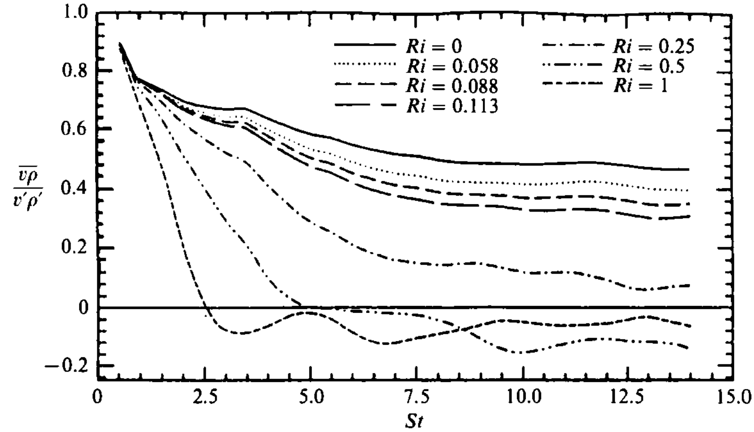

FIGURE 15. Evolution of the vertical density flux as a function of Richardson number.

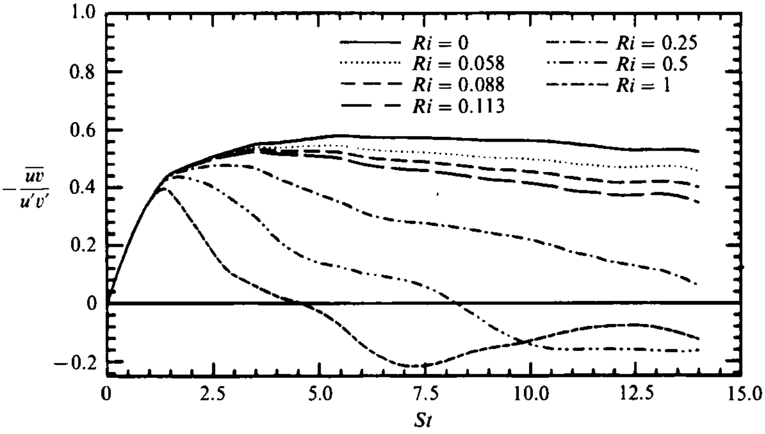

FIGURE 16. Evolution of the Reynolds stress as a function of Richardson number.

large St. This criterion is equivalent to those of maximum energy partition and maximum anisotropy as will be shown below.

The physical significance of Ri_t is that this Richardson number signals a change from shear driven turbulence to buoyancy dominated turbulence. In the h series simulations discussed above $Ri_t \approx 0.25$. The correspondence of $Ri_t \approx 0.25$ with the critical Richardson number for inviscid stability is coincidental and will be explained as a Reynolds number effect in § 5.3.

When comparing the results in figures 15–17 with the equivalent figures in Gerz *et al.* (1989) and Gerz & Schumann (1991) the following trends are apparent. All three sets of simulations are in good agreement for $\overline{uv}/u'v'$ and $\overline{u\rho}/u'\rho'$ (the magnitude of these quantities predicted by Gerz simulations is slightly lower) but the simulations of Gerz *et al.* (1989) are significantly different from those of Gerz & Schumann (1991) and these simulations when considering the $\overline{v\rho}/v'\rho'$ quantity. Not only are the magnitudes of this correlation much lower in the Gerz *et al.* simulations but the time to zero crossing for the $Ri = 0.5$ and 1.0 cases predicted by their simulations is much shorter. It is distinctly possible that the initial differences in this correlation are due to the fact that η_0 is equal to 0 for the results of Gerz & Schumann and those shown in figure 15, whereas the corresponding value in the simulations of Gerz *et al.* is 1.

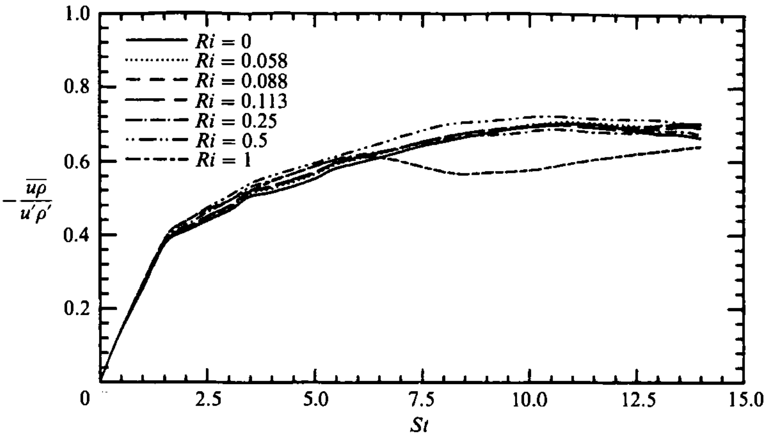

FIGURE 17. Evolution of the streamwise density flux as a function of Richardson number.

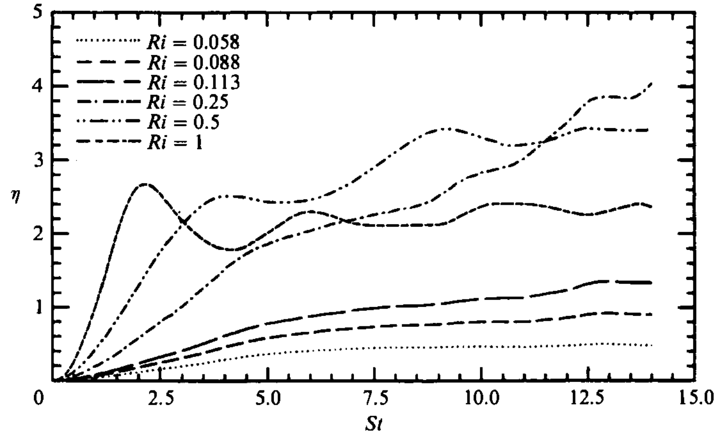

FIGURE 18. Evolution of the energy partition as a function of Richardson number.

However, as shown in figures 28 and 29 (see §6) the fluxes become independent of η_0 at later times in the simulation. The difference at later times, then, is probably due to Prandtl number effects: Gerz *et al.* used a *Pr* of 5.0 in their simulations as compared to the value of 1.0 in our simulations and those of Gerz & Schumann. For example, in figure 31 it can be seen when *Pr* (or *Sc*) is increased for $Ri = 0.5$ in our simulations the time to zero crossing decreases and agreement with Gerz *et al.*'s results improves. The *Re* effects on the fluxes shown in figures 15–17, especially at larger times, appear to be minimal. For example if we compare the results shown in figure 4 (high *Re*, table 5) with those in figure 15 (lower *Re*, table 1) we see that not only are the magnitudes of the fluxes very similar at larger values of *St* for all *Ri*, but the time to zero-crossing for the $Ri = 1$ case is identical in both figures.

Since the vertical density flux reflects the exchange of energy between *PE* and *VKE* it is of interest to investigate the ratio of these two forms of energy as a function of *Ri*. (Note that in this context the potential energy we refer to is the *available* potential energy.) As shown in figure 18, the energy partition, $\eta = PE/VKE$, approaches a constant at large *St* for fixed *Ri*. (There is some uncertainty in the asymptotic behaviour of η at $Ri = 0.25$ owing to the limited *St* attainable in the simulations.) In the case of DG fluxes ($Ri < Ri_t$), *VKE* is gained indirectly from

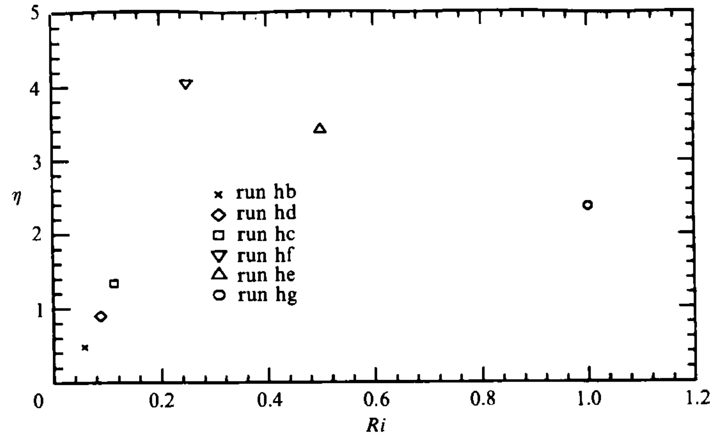

FIGURE 19. The energy partition as a function of Richardson number.

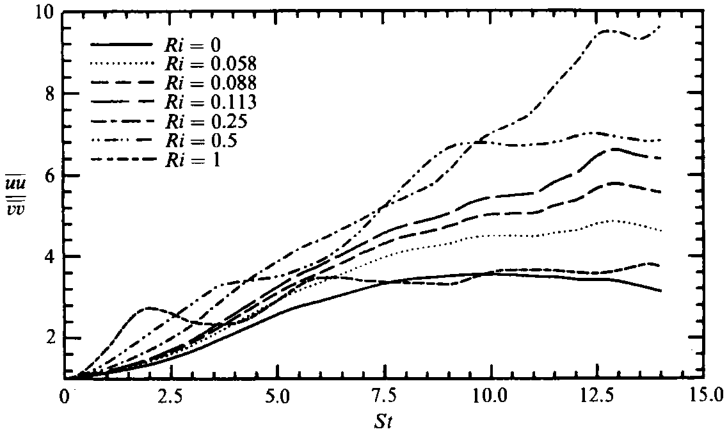

FIGURE 20. Evolution of $\overline{uu}/\overline{vv}$ as a function of Richardson number.

production through pressure–strain redistribution. This *VKE* is converted to *PE*, some of which is dissipated and η becomes constant. In the case of CG fluxes ($Ri > Ri_t$), the *PE* gained while the vertical density flux is DG is later converted back to *VKE* with the appearance of the CG vertical density flux. Some of this *VKE* is then dissipated or redistributed to $\overline{uu}$ and η again becomes constant. Note that the condition of constant η occurs independently of how the constituent energies evolve. For $Ri < Ri_s$ both forms of energy grow whereas for $Ri > Ri_s$ both forms decay.

As shown in figure 19, η increases with increasing Ri, up to $Ri_t = 0.25$, then decreases slightly. For increasing $Ri < Ri_t$ the decreasing amount of *VKE* produces increasing levels of *PE*. Evidently, in a more strongly stratified flow a given $\overline{vv}$ results in a larger $\overline{\rho\rho}$. This efficient production of *PE* also occurs at $Ri > Ri_t$ as long as $\overline{v\rho}/v'\rho' > 0$. However, the production of *PE* ceases when the flux reversal occurs and buoyancy forces reconvert *PE* to *VKE*. As Ri increases the flux reversal occurs earlier and the asymptotic value of η decreases slightly.

The CG fluxes also affect the distribution of turbulent kinetic energy among the three velocity components. To investigate this the ratio $\overline{uu}/\overline{vv}$ is shown as a function of time in figure 20. At $Ri = 0$, $\overline{uu}$ is greater than $\overline{vv}$ owing to the direct effect of

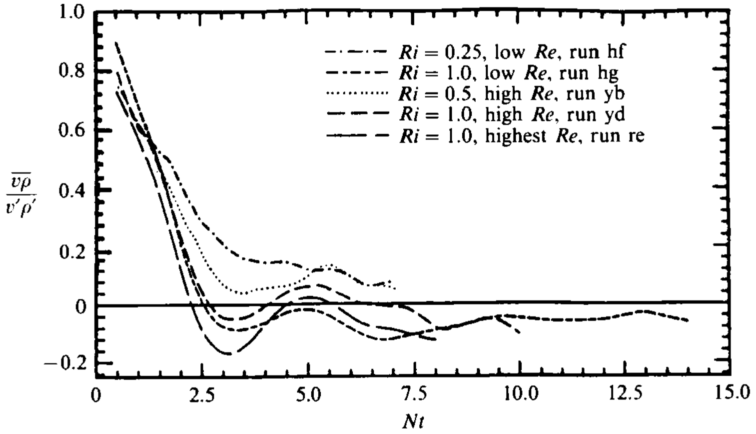

FIGURE 21. Evolution of the vertical density flux at large Richardson number.

production on $\overline{uu}$. As Ri increases in the range $0 < Ri < Ri_t$, the anisotropy increases. Although both $\overline{uu}$ and $\overline{vv}$ decrease owing to the suppression of production, the conversion of *VKE* to *PE* further decreases $\overline{vv}$. For $Ri > Ri_t$ the anisotropy decreases with increasing Ri, where the CG vertical density flux signals a return of *PE* to *VKE* (thus increasing $\overline{vv}$) and the associated reversal in production reduces $\overline{uu}$.

Figure 20 also reveals a weak tendency toward isotropy at large St in the $Ri = 0$ case. This is presumably a consequence of increasing Reynolds number. Rogers *et al.* (1986) also found increased isotropy in successive simulations of increasing Re at $Ri = 0$. These results are not surprising since more of the scales contributing to $\overline{uu}/\overline{vv}$ should be isotropic at larger Re. The implication is that part of the increase in anisotropy with increasing $Ri < Ri_t$ in figure 20 is due to a decrease in Re (for fixed initial conditions). However, the decrease in anisotropy for $Ri > Ri_t$ at even lower Re is a genuine effect of stratification.

5.3. *Behaviour at large Richardson number*

5.3.1. *Brunt–Väisälä frequency scaling*

In the definition $Ri = N^2/S^2$ both the BV frequency and the mean shear rate have dimensions of t^{-1}. This suggests a multiple mean timescale problem. At large Ri, N should be the more important timescale so we now consider the behaviour of the normalized fluxes as functions of Nt at large Ri.

In figure 21, $\overline{v\rho}/v'\rho'$ is shown as a function of Nt for several Ri and Reynolds numbers. For $Ri = 1.0$ the zero crossing occurs at $Nt \approx 2.4$ and is nearly independent of Re. The time to zero crossing of $\overline{v\rho}/v'\rho'$ according to the inviscid rapid distortion analysis of Hunt *et al.* (1988) is $Nt = 2.0$, whereas in the unsheared, stratified flow studies of Riley *et al.* (1981) and Itsweire *et al.* (1986), the first zero crossing occurs at $Nt \approx 3.0$. In the simulations of Riley *et al.* (1981) and the unsheared linear theory of Hunt *et al.* (1988) the vertical density flux oscillates about zero at approximately half the BV period. In the present study the temporal mean of $\overline{v\rho}/v'\rho'$ at $Ri = 1.0$ is slightly negative after the first zero crossing, signalling a net conversion of *PE* to *VKE*. However, this mean value is modulated by oscillations at approximately the same period found in the unsheared studies. In the high-Reynolds-number y and r series simulations at $Ri = 1.0$ the oscillatory modulations are sufficiently large to

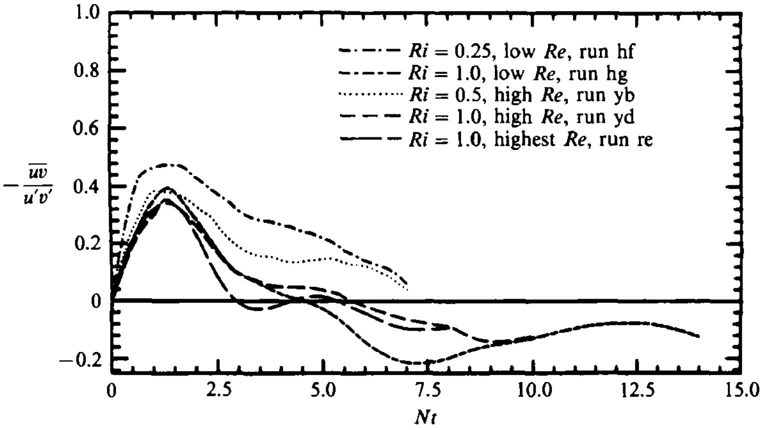

FIGURE 22. Evolution of the Reynolds stress at large Richardson number.

cause two zero crossings and therefore a temporal reversal in the exchange of *PE* and *VKE*.

Figure 21 also illustrates that in the large-Reynolds-number y series simulation at $Ri = 0.5$, $\overline{v\rho}/v'\rho'$ approaches zero but does not become CG. This suggests that $Ri_t \approx 0.5$ *in these larger Re* runs. Apparently, Ri_t increases with increasing Re. The existence of flux reversals at $Ri = 1.0$ in the largest Reynolds number r series simulations (where $Ri_s \approx 0.21$) further suggests that the upper bound on Ri_t may be 1.0.

As shown in figure 22, the initial peak in $-\overline{uv}/u'v'$ occurs at $Nt \approx 1.2$–1.5, independent of Ri and Re. The peak in *PE* also occurs at $Nt \approx 1.5$ and is fairly independent of Ri and Re. This suggests a characteristic time to the onset of the effects of stable stratification. The rapid distortion analysis of Hunt *et al.* (1988) predicts a characteristic time of $Nt = 1.0$ whereas the unsheared experiments of Itsweire *et al.* (1986) give $Nt \approx 1.7$.

5.3.2. *Small-scale flux reversals*

The temporal reversals in the globally averaged fluxes $\overline{v\rho}/v'\rho'$ and $-uv/u'v'$ are also evident in the co-spectra of figures 23 and 24. Initially, the most energetic modes are DG but later they exhibit a reversal. In contrast, the higher-wavenumber modes are persistently CG. (The temporal decrease in the absolute value of the flux at each wavenumber is due to the flow becoming less energetic. This effect can be partly compensated for by small-scale normalization, see Holt 1990.)

The persistent CG flux at large wavenumbers is probably a Reynolds-number effect. According to the Kolmogorov hypotheses the small-scale motions are isotropic at large *Re* so that the co-spectra at large wavenumbers should be zero. Experimental studies support the argument that the persistent CG flux is an *Re* effect. The unsheared air-flow studies of Lienhard & Van Atta (1990) and Yoon & Warhaft (1990) show no small-scale reversal. The shear-flow results of Rohr *et al.* (1988*b*) and the unsheared data of Itsweire & Helland (1989) both show inconclusive evidence of the small-scale reversal. In any case the magnitude of the reversal is insignificant at the Reynolds numbers of the latter experiments. See also Gerz *et al.* (1989) who present an alternative argument for the Reynolds-number dependence of the small-scale reversals in terms of dissipation rates.

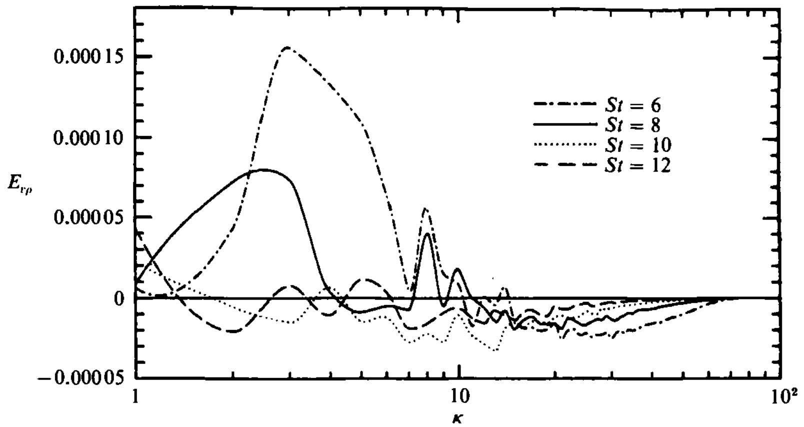

FIGURE 23. The radial co-spectra of the vertical density flux at $Ri = 0.5$.

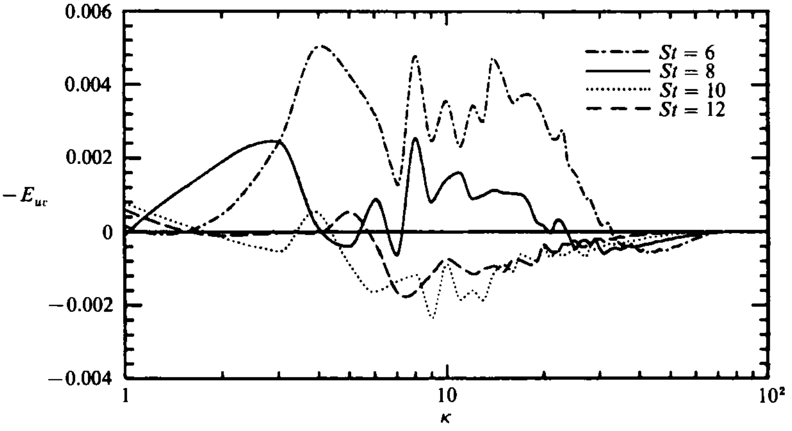

FIGURE 24. The radial co-spectra of the Reynolds stress at $Ri = 0.5$.

Even if the small-scale reversal is limited to low Reynolds numbers the effects are apparently not significant. If they were, the globally averaged fluxes would change sign earlier in the smaller *Re* cases. However, this effect was not conclusively observed in §5.3.1. In addition, the time to reversal, $Nt \approx 2.4$, reported here is slightly greater than the $Nt = 2$ predicted by inviscid rapid distortion analysis (Hunt *et al.* 1988) in which there are no small scale reversals (Holt 1990).

5.3.3. *Turbulence or internal waves?*

The transfer spectra presented in §5.1 showed that for large *Ri* the spectral transfer is essentially zero (see figure 14). Two interpretations may be drawn from this result. The first is that at large *Ri* the flowfield possibly consists primarily of linear internal waves and the second is that the flow field consists of linear buoyancy-driven motions. Let us treat each possibility in turn.

As pointed out by Stewart (1969), $\overline{v\rho} = 0$ in a linear internal wave field. In the unsheared experiments of Stillinger *et al.* (1983), $\overline{v\rho}/v'\rho'$ vanished, which led those investigators to conclude that internal waves were present. (However, $\overline{v\rho} = 0$ is not a sufficient condition for the existence of internal waves.) In our large *Ri* simulation

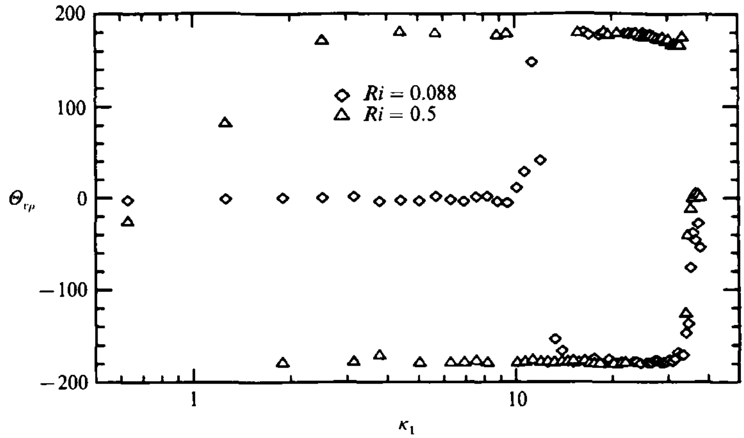

FIGURE 25. Phase angle of the vertical velocity and density at $St = 12$.

results, $\overline{v\rho}/v'\rho'$ is nearly zero, although very weakly negative when averaged over the whole simulation.

Komori *et al.* (1983) studied the phase relationship between the vertical velocity and temperature in a stably stratified channel flow. Their results supported the existence of a large scale CG vertical heat flux superposed on an internal wave field. However in their study of thermally stratified unsheared turbulence Lienhard & Van Atta (1990) showed that the phase correlations were not consistent with the existence of internal waves even though $\overline{vT} \approx 0$. In addition, their success in collapsing their spectra using Kolmogorov scaling certainly brings into question the use of $\overline{v\rho} = 0$ as a criterion for inferring (linear) internal waves.

The phase correlations between the vertical velocity and the density, $\Theta_{v\rho}$, in the present simulations at $St = 12$ are shown in figure 25. At $Ri_s = 0.088$, $\Theta_{v\rho} \approx 0$ at the most energetic wavenumber. Thus, v and ρ are in phase, consistent with the shear driven DG vertical density flux. At larger wavenumbers v and ρ are $\pm 180°$ out of phase, owing to small-scale flux reversals (see also §7). At large $Ri = 0.5$, $\Theta_{v\rho} \approx \pm 180°$ at nearly all wavenumbers, consistent with the buoyancy-driven CG vertical density flux. Thus, the phase relations shown in figure 25 lead us to the second interpretation implied by reduced transfer, that at large Ri the flow consists mainly of linear buoyancy-driven motions. At large Ri only the lowest wavenumbers exhibit $\Theta_{v\rho} \approx \pm 90°$, suggestive of large-scale internal waves. Further investigations including conditional sampling (Komori *et al.* 1983) may provide more conclusive evidence of internal waves.

The transition from shear-driven DG fluxes to buoyancy-driven CG motions is also apparent in the instantaneous density profiles. A DG vertical density flux is caused by the lifting (descent) of heavy (light) fluid into lighter (heavier) fluid. The flux may also be sufficiently strong to produce a local instability in the total density ($\varrho = \rho_0 + S_\rho y + \rho$) profile. An instability is a region in which heavy fluid overlies light fluid, i.e. $\partial\varrho/\partial y > 0$. Such an instability offers substantial opportunity for turbulent mixing. (Here, mixing is the reduction of local density gradients.) In contrast, a weaker flux produces smaller local density gradients which will be reduced primarily through molecular diffusion.

The total density profiles were inspected for instabilities over a range of Ri. One such profile at $Ri_s = 0.088$ and $St = 12$ is shown in figure 26 wherein instabilities of

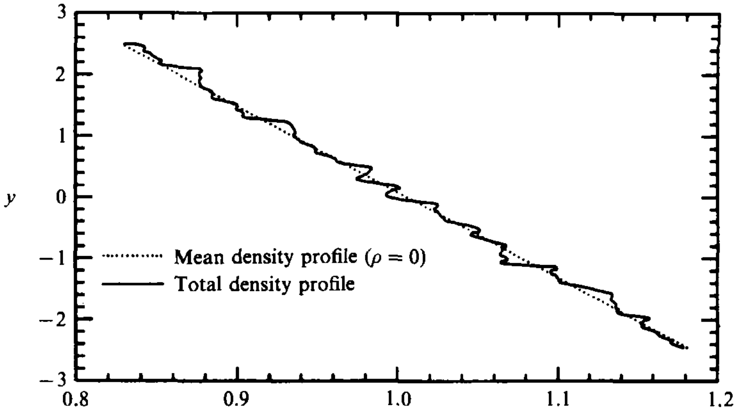

FIGURE 26. Total density profile at $Ri_s = 0.088$ and $St = 12$.

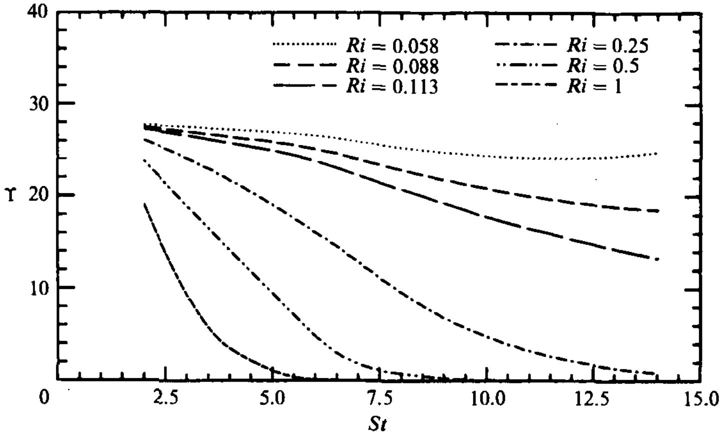

FIGURE 27. Evolution of the instability percentage as a function of Richardson number.

varying scale are evident. The profile also contains several statically stable deviations from the mean density.

The percentage of instabilities, Υ, within the entire database at a fixed Ri and St was then computed. This was accomplished by dividing the total number of instabilities found in all profiles by the total number of stability tests. (A test was conducted between all pairs of neighbouring grid points in each profile.) Note that Υ does not accurately measure the percentage of turbulent events that produce instabilities, as one large-scale event may contain or produce several smaller-scale instabilities (see figure 26). Nonetheless, Υ is the fraction of the flow field that is statically unstable.

As shown in figure 27, Υ decreases with increasing Ri. This result may be interpreted as follows. For $Ri < Ri_t$ the reduction in instabilities is due to the suppression of turbulence production which results in less intense DG vertical density fluxes. For $Ri > Ri_t$ the number of instabilities rapidly approaches zero. By synthesizing the latter observation with those obtained from the phase correlations we postulate that at large Ri the flowfield consists mainly of low intensity buoyancy driven motions that are incapable of producing instabilities and, possibly, large scale internal waves that do not break.

6. Effects of other parameters

In previous sections we characterized the flow in terms of the Richardson and Reynolds numbers. In this section we discuss the effects of two other dimensionless parameters: the initial energy partition and the Schmidt (Prandtl) number.

6.1. *Initial energy partition variation*

The amount of potential energy will differ in turbulence generated by shear instability compared to that generated by density instability. It is therefore important to understand the effects of varying η_0, the initial ratio of *PE* to *VKE*.

In their linearized analysis of unsheared stratified turbulence Hunt *et al.* (1988) found that when η_0 was increased from 0 to 1 the amplitudes of the oscillations in the *VKE*, the *PE*, and $\overline{v\rho}$ were approximately 30 % of those in the $\eta_0 = 0$ case. However, Gerz & Schumann (1989) found that in the presence of shear the asymptotic values of $-\overline{uv}/v'v'$ and $\overline{vT}/v'T'$ were not significantly affected as η_0 was increased from 0 to 0.5 at $Ri = 1.0$. This insensitivity is not too surprising since Gerz & Schumann (1989) varied η_0 over a smaller range than used in this study.

In our study η_0 was prescribed as follows. From our simulation results with $\eta_0 = 0$ we noted the asymptotic value, η_a, of the energy ratio as a function of *Ri*. Then we repeated the simulations with $\eta_0 = 2\eta_0$. Specifically, the *h* series simulation results ($\eta_0 = 0$) at $Ri_s = 0.088$ and $Ri = 0.5$ were compared to the *e* series simulation results at $Ri = 0.088$ with $\eta_0 = 2$, and at $Ri = 0.5$ with $\eta_0 = 7$.

The disadvantage of this approach is that the total initial energy, $E_t = \frac{1}{2}q_0^2\,(1+\frac{1}{2}\eta_0)$, increases as η_0 increases. We could overcome this problem by fixing E_t. However, the necessary change in q^2 would introduce Reynolds-number and dimensionless-shear-rate effects.

We will show that in both the shear-driven case ($Ri = 0.088$) and the buoyancy-dominated case ($Ri = 0.5$) the qualitative behaviour of the developed flow is not significantly changed by the variation in η_0. However, the paths by which the flows develop exhibit differences.

At $Ri = 0.088$ the parameter $F = (\mathscr{P}-\mathscr{B})/\epsilon$ was approximately 7 % larger throughout the simulation when η_0 was increased from 0 to 2. Given that Ri_s corresponds to $F \approx 1$ this implies that Ri_s is slightly greater than 0.088 when $\eta_0 = 2$. Thus, we expect to have a larger Reynolds number. Indeed, for $St > 5$ the component kinetic energies, $\frac{1}{2}\overline{u_\alpha u_\alpha}$, are approximately 20 % larger in the $\eta_0 = 2$ case. This may be explained as follows.

When $\eta_0 = 0$ significant *VKE* is expended to create *PE* at small *St*. Also, some of the streamwise kinetic energy gained through production is distributed to *VKE* and, in turn, maintains the conversion of *VKE* to *PE*. When $\eta_0 = 2$ significant initial *PE* already exists and, as a result, the energy in the velocity field is retained. Hence, the 20 % increase in $\frac{1}{2}\overline{u_\alpha u_\alpha}$. A 20–30 % increase in the component kinetic energies was also observed in the unsheared results of Hunt *et al.* (1988) when η_0 was increased from 0 to 1.

At $Ri = 0.088$ and $St > 5$ the qualitative behaviour of η is relatively independent of η_0 (see figure 28). However, η_a is slightly smaller with increased η_0. The reduction in η_a is consistent with the tendency for η_a to decrease with decreasing *Ri*, for $Ri < Ri_t$ (refer to figure 19). The more energetic case of $\eta_0 = 2$ has a lower effective *Ri* and so exhibits a lower η_a.

In §5.2 we also showed that at $Ri_s = 0.088$ and $\eta_0 = 0$ the vertical density flux is DG for all *St*. However, when $\eta_0 = 2$ the flux is weakly CG at small *St* (see figure 29).

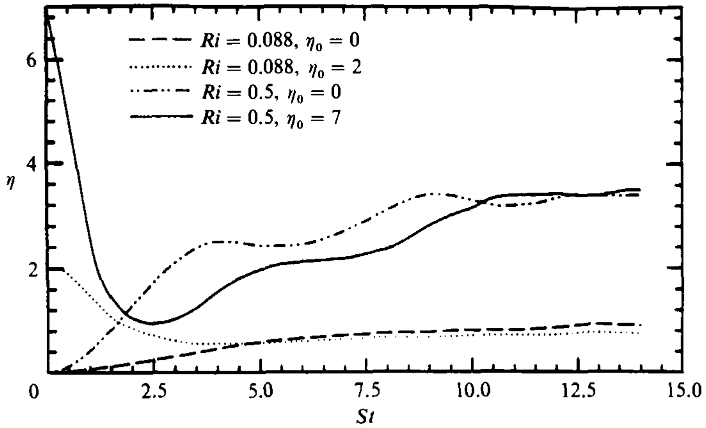

FIGURE 28. Evolution of the energy partition as a function of its initial value.

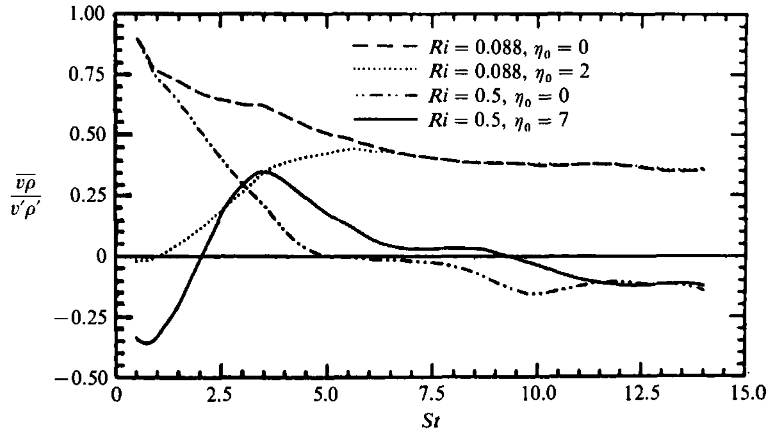

FIGURE 29. Evolution of the vertical density flux as a function of the initial energy partition.

In this case, $\eta_0 > \eta_a$ and some of the excess initial *PE* is converted to *VKE* to resolve the initial imbalance in η. This energy conversion causes the transient CG flux. Thereafter, $\overline{v\rho}/v'\rho'$ develops essentially as in the $\eta_0 = 0$ case. The Reynolds stress is, however, DG for all time when $\eta_0 = 2$. In this case, $-\overline{u\rho}/u'\rho'$ is reduced at small *St*, so the energy conversion that creates the CG vertical density flux does not affect the Reynolds stress.

We now consider the effect of η_0 upon the buoyancy-dominated ($Ri > Ri_t$) case. An increase in η_0 at $Ri = 0.5$ results in effects similar to those observed at $Ri = 0.088$. For example, when η_0 is increased from 0 to 7 the developed flow is more energetic; both the component kinetic energies and the *PE* increase. The initial imbalance in η again results in a transient CG vertical density flux at small *St* (figure 29) and a reduction in $-\overline{u\rho}/u'\rho'$. The significant initial conversion of *PE* to *VKE* at $\eta_0 = 7$ also results in a smaller η at intermediate times, although η_a is essentially unaffected (figure 28).

The increase in η_0 at $Ri = 0.5$ also delays the time to the second CG flux (see figure 29). This is consistent with the proposition that Ri_t increases with increasing Reynolds number. Presumably, at sufficiently large η_0 the flux reversal would not

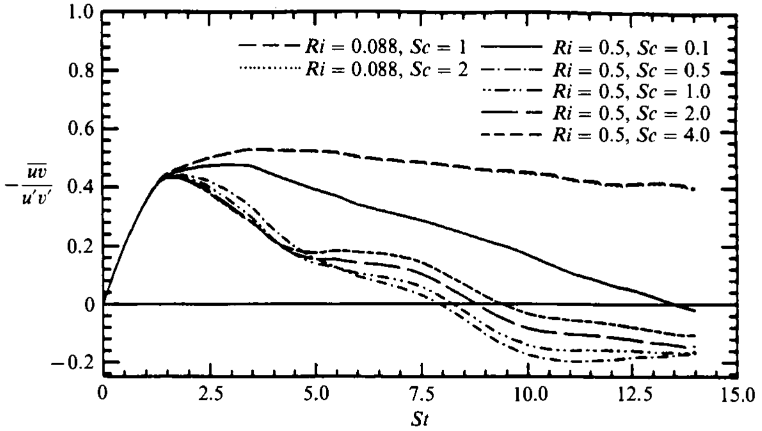

FIGURE 30. Evolution of the Reynolds stress as a function of the Schmidt number.

occur at $Ri = 0.5$ and, by definition, $Ri_t \approx 0.5$. The flow would also be more energetic, i.e. of larger Re than the case of $\eta_0 = 0$ where $Ri_t = 0.25$ (see §5.2).

6.2. *Schmidt (Prandtl) number variation*

The range of Prandtl and Schmidt numbers found in the oceans, the atmosphere, and fresh-water bodies cause the dissipation of the various scalars to behave differently and may affect the vertical fluxes. In this section we investigate the effects of Sc variation. Specifically, in the shear-dominated case of $Ri_s = 0.088$ we discuss the effects of increasing Sc from 1.0 to 2.0, and in the buoyancy dominated case of $Ri = 0.5$ we examine the effects of increasing Sc from 0.1, to 0.5, 1.0, 2.0, and 4.0. Specification of a larger Sc is precluded by the requirement of adequate resolution of the scalar dissipation. However, the limited attainable Sc allows us to study the qualitative effects of this parameter.

At $Ri_s = 0.088$ the increase in Sc from 1.0 to 2.0 causes a 2% decrease in $F = (\mathscr{P} - \mathscr{B})/\epsilon$. Although the range of Sc studied here is rather small we can infer that F and thus Ri_s may be insensitive to Sc (for $Sc \geqslant 1$). This is expected since $F \approx \mathscr{P}/\epsilon$ and $\mathscr{P}/\epsilon$ is primarily determined by the velocity field. Indeed, at $Ri_s = 0.088$ the normalized Reynolds stress is essentially unchanged by the increase in Sc (see figure 30). Furthermore, in the analysis of §5.1 we explained how $\mathscr{L}$ and thus Sc do not affect Ri_s significantly.

The slight decrease in F with increasing Sc at Ri_s may be explained as follows. A DG Reynolds stress event not only exchanges momentum but also lifts heavy fluid into lighter ambient fluid (or vice versa). During this process the scalar diffusion may reduce the buoyancy of the fluid parcel. As Sc increases the scalar diffusion decreases and the parcel remains strongly buoyant, effectively increasing the influence of stratification and weakening the scalar production event. This argument is supported by the fact that at $Ri_s = 0.088$, $\overline{v\rho}/v'\rho'$ decreases with increasing Sc (figure 31); similar changes in $\overline{v\rho}/v'\rho'$ occur as the strength of the stratification, or Ri, increases at fixed Sc and $Ri < Ri_t$ (see §5.2).

We now consider the effect of increasing Sc upon the buoyancy dominated case ($Ri > Ri_t$). At $Ri = 0.5$ the normalized CG vertical density flux becomes stronger as Sc increases from 0.5 to 4.0 (see figure 31). The time to the flux reversal also decreases with increasing Sc. These effects may be explained as follows. As Sc increases the

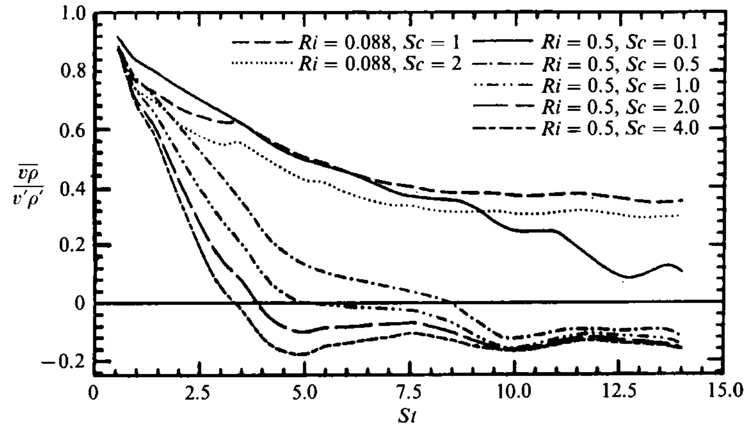

FIGURE 31. Evolution of the vertical density flux as a function of the Schmidt number.

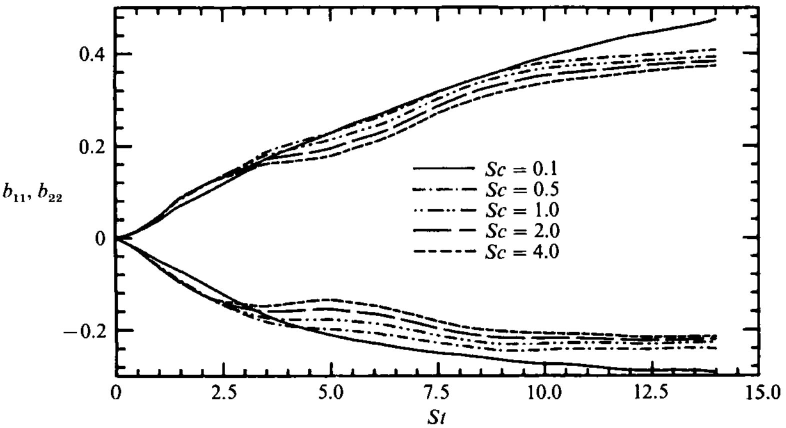

FIGURE 32. Evolution of b_{11} and b_{22} as a function of the Schmidt number at $Ri = 0.5$.

buoyant fluid parcels retain their density deviations longer and are more strongly affected by gravity, which returns the fluid parcel to a neutrally buoyant position. For $Sc = 0.1$, the density of the fluid parcels is so strongly diffused that no CG flux occurs.

The effects of Sc on $\overline{v\rho}/v'\rho'$ imply that Ri_t increases with decreasing Sc. Recall from §5.2 that Ri_t is defined, in part, by the condition of zero $\overline{v\rho}/v'\rho'$ at large St. At $Sc \approx 0.1$ we find that $Ri_t \approx 0.5$ whereas $Ri_t \approx 0.25$ at $Sc = 1$ (see §5.2). The effect of Sc variation upon Ri_t is expected to decrease with increasing Reynolds number.

The Reynolds stress behaviour at $Sc = 0.1$ (figure 30) is similar to that of $\overline{v\rho}/v'\rho'$ despite the fact that the correlation, $\overline{u\rho}/u'\rho'$, between light and fast fluid (or slow and heavy fluid) is relatively low at this Sc. In contrast to the behaviour of $\overline{v\rho}/v'\rho'$ the time to the Reynolds stress reversal increases with increasing Sc and the subsequent CG Reynolds stress is weaker. Although u and ρ remain strongly correlated as Sc increases, differences in the behaviour of $\overline{uv}/u'v'$ and $\overline{v\rho}/v'\rho'$ exist. Differences in the pressure–strain and pressure–density gradient mechanisms and the respective dissipation rates may be relevant in this regard.

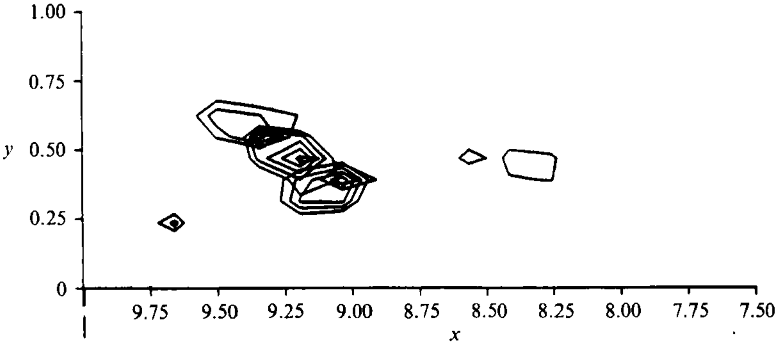

FIGURE 33. Side view of a DG Reynolds stress ($-uv > 0$) event at $Ri_s = 0.088$ and $St = 12$.

The effects of Sc on the anisotropy in the velocity field are reflected by the tensor

$$b_{ij} = \frac{R_{ij}}{R_{kk}} - \tfrac{1}{3}\delta_{ij}. \tag{44}$$

As shown in figure 32 the anistropy decreases (decreasing b_{11} and $|b_{22}|$) with increasing Sc. Essentially the same trends and magnitudes were obtained by Gerz *et al.* (1989) for b_{11} and b_{22}. The agreement between their results and ours is good over a range of Ri from 0 to 1. As Sc increases the increasingly buoyant fluid parcels return more PE to VKE and $|b_{22}|$ decreases, as does b_{11} since $b_{ii} = 0$. This is consistent with the behaviour of $\overline{v\rho}/v'\rho'$ in figure 31 where, at larger Sc, the CG flux occurs earlier and is stronger, reflecting the return of more PE to VKE. The CG Reynolds stress also decreases b_{11} since the production becomes negative. Although the (normalized) CG Reynolds stress becomes weaker as Sc increases (figure 30), in the present buoyancy-dominated case this effect is not significant enough to increase b_{11}.

7. Coherent structure

Our goal in this section is to describe, in terms of coherent vorticity, the dynamics of the local DG and CG fluxes. These fluxes, in turn, determine the behaviour of the averaged fluxes described in previous sections.

7.1. *Structure at small Richardson number*

We first describe the structure in the shear dominated ($Ri < Ri_t$) case. A side view of contour surfaces of DG Reynolds stress ($-uv > 0$) in the h series simulation at $Ri_s = 0.088$ and $St = 12$ is shown in figure 33. Only the most intense flux in the sampling volume is shown. Owing to the correlation of light fluid with fast fluid and heavy fluid with slow fluid (see §5.2) the contour surfaces of $v\rho$ resemble those of uv. Inspection of the velocity and density contours in this region shows that these fluxes are composed of light ($\rho < 0$), fast ($u > 0$) fluid moving downward ($v < 0$) into slow, heavy fluid.

To investigate coherent vorticity in the neighbourhood of these fluxes, vorticity line tracings were initiated near the fluxes. These vortex lines are simply trajectories, $r_i(s)$, with slope, $\mathrm{d}r_i/\mathrm{d}s$, parallel to the local fluctuating vorticity vector, ω_i. As shown in figure 34 the coherent vorticity lines resemble a hairpin. The head is located at the upper left with the two legs branching off the head. In this example the legs are connected at the lower right by extremely weak vorticity. The vorticity direction

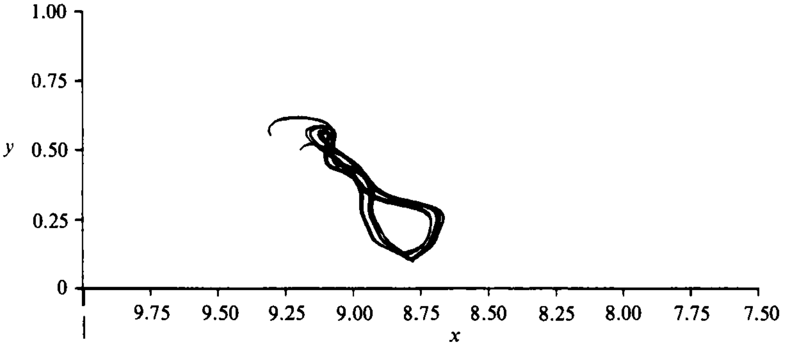

FIGURE 34. Side view of the vorticity lines in vicinity of the flux of figure 33.

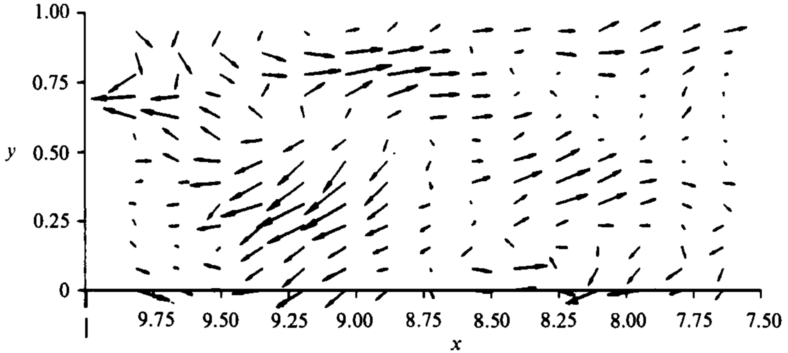

FIGURE 35. Velocity vectors in the mid-plane of the structure of figure 34.

along the right-hand leg is toward the head and away from the head along the opposite leg. The associated fluid motion can be inferred from the left-hand rule (where the thumb of the left hand is aligned with the vorticity and the fingers are curled in the direction of the fluid velocity). The fluid motion so determined implies that fluid is pumped (Rogers *et al.* 1986) downward through the centre of the hairpin: light, fast fluid from above the hairpin is moved downward into ambient slow, heavy fluid, resulting in the DG fluxes.

Hunt (1978) explained that a spanwise vortex element which is perturbed into the direction of expansive strain (see §2.3) may be stretched into a hairpin shape. As shown in figure 34 the legs of the hairpin are inclined approximately 45° to the horizontal; this is consistent with the direction of expansive strain. As discussed by Rogers *et al.* (1986), the inclination angle can be reduced by the mean rotation and in some cases may be approximately 20°. The side view in figure 34 also provides a sense of scale of the hairpin; the vertical and streamwise dimensions of the computational domain are approximately 5 and 10 units.

By comparing figures 33 and 34 we see that the DG flux resides just below and downstream of the head and the upper regions of the legs. This is consistent with the pumping mechanism explained above. Indeed, the velocity field in a vertical (x, y)-plane passed between the legs of the hairpin (figure 35) clearly shows that fluid is moving downward through the hairpin.

We can further investigate the hairpin structure by projecting the fields onto planes. Since the hairpins are thought to evolve from the expansive straining of

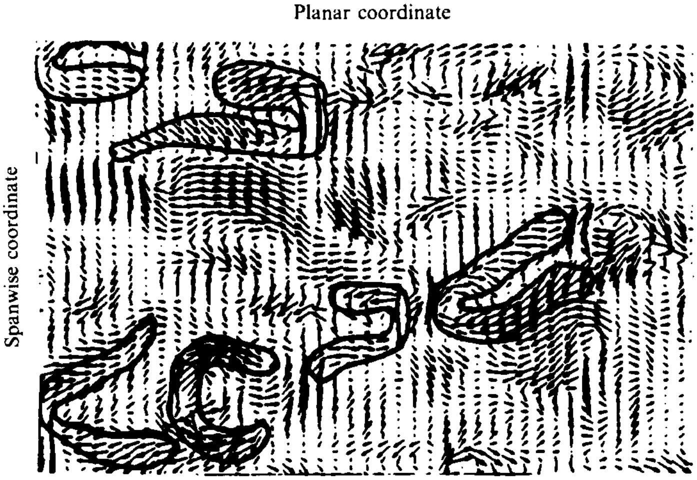

FIGURE 36. Vorticity vectors projected onto a plane inclined 26.6° from the horizontal at $Ri_s = 0.088$ and $St = 12$.

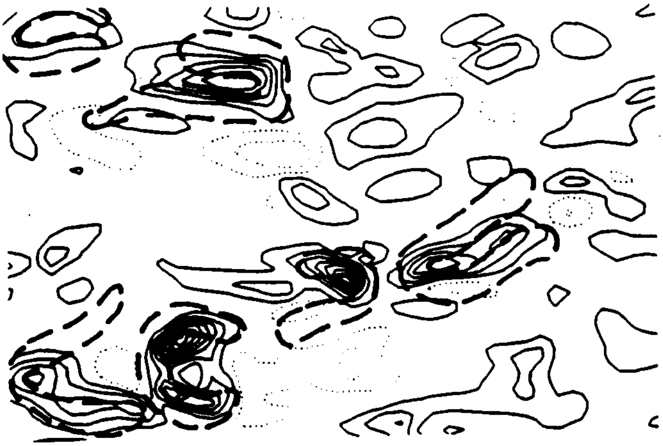

FIGURE 37. Contours of the Reynolds stress in the plane of figure 36. Solid (dotted) contours correspond to DG (CG) fluxes. Dashed lines are from figure 36.

vortex elements it is of interest to calculate the inclination angle, θ, of the vorticity vectors from the horizontal (Moin & Kim 1985). At $Ri = 0$ and $Ri_s = 0.088$ intense vorticity is typically inclined at $\theta \approx 20°\text{–}40°$ and, of course, at $180°\text{–}\theta$ (Holt 1990). This suggests that the vorticity field may be accurately depicted by projection onto a plane inclined 26.6° (a computationally convenient value) from the horizontal.

The projection shown in figure 36 at $Ri = 0.088$ and $St = 12$ reveals several hairpin structures with heads at either the upstream or downstream ends. Similar results have been obtained by Rogers *et al.* (1986) and Gerz (1989). As expected, the hairpins of figure 36 correlate with DG Reynolds stresses (figure 37) and vertical density fluxes.

At both $Ri = 0$ and $Ri = Ri_s$ regions of instantaneous CG Reynolds stress and vertical density flux can be identified (see figure 37 for example). At $Ri = 0$ the CG fluxes must be due to the local turbulence, and not buoyancy forces. When a fast

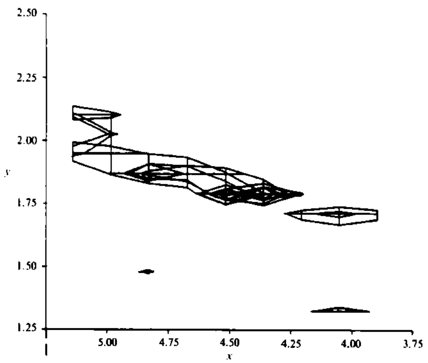

FIGURE 38. Side view of a CG vertical density flux ($v\rho < 0$) at $Ri = 0.5$ and $St = 12$.

(slow) fluid parcel is pumped downward between the legs of a hairpin, part of the parcel may be caught in the vortex motion of one leg and returned toward fast (slow) fluid, resulting in a local CG flux. Indeed, CG regions are observed outside the legs, as well as outside the heads. These small scale CG fluxes become stronger at $Ri = Ri_s$, being reinforced by buoyancy forces. However, CG fluxes also occur in regions removed from hairpins. A DG fluid parcel formed through pumping may later move away from generating hairpin. The parcel will then become CG under the influence of gravity. The small-scale CG fluxes discussed here are also evident in the radial co-spectra of figure 13 and the phase correlations of figure 25.

For additional description of the hairpin structure see the stratified homogeneous shear flow results of Holt (1990), Holt, Koseff & Ferziger (1989), and Gerz (1989), the unstratified homogeneous shear flow results of Rogers *et al.* (1986), and the unstratified inhomogeneous results of Robinson (1990), Moin & Kim (1985), and Head & Bandyopadhyay (1981). Robinson (1990) and Holt (1990) also discuss the relevance of the pressure field to coherent vorticity structures.

7.2. *Structure at large Richardson number*

The instantaneous fields have also revealed the structure of the large-scale CG fluxes. The structure described here was found in the buoyancy dominated *h* series simulated at $Ri = 0.5$ and $St = 12$. Similar structures were observed at $Ri = 1.0$ in both the *h* series and the higher-Reynolds-number *y* series fields.

A side view of an intense CG vertical density flux ($v\rho < 0$) is shown in figure 38. The significant correlation between u and ρ produces a visually similar CG Reynolds stress ($-uv < 0$). These fluxes are composed of light ($\rho < 0$), fast ($u > 0$) fluid moving upward ($v > 0$). Thus we infer that light fluid is travelling up toward a position of neutral buoyancy. However, the motion is not vertically upward as might be expected in the presence of stratification alone. Instead, as shown in figure 38, the CG parcel is inclined approximately 15° to the horizontal. Prior to the appearance of the CG fluxes the significant conversion of *VKE* to *PE* and the production of streamwise velocity fluctuations results in fluid motions that are nearly horizontal. The mean rotation may also reduce the inclination angle from that of expansive straining of the CG fluid.

The CG fluid parcel induces vorticity along its perimeter as it moves through the ambient fluid and the resulting vortex lines form a helical structure as shown in figure 39. The counterclockwise sense of these vorticity lines is consistent with the proposition that the buoyant parcel induces vorticity in its wake (recall the left-hand

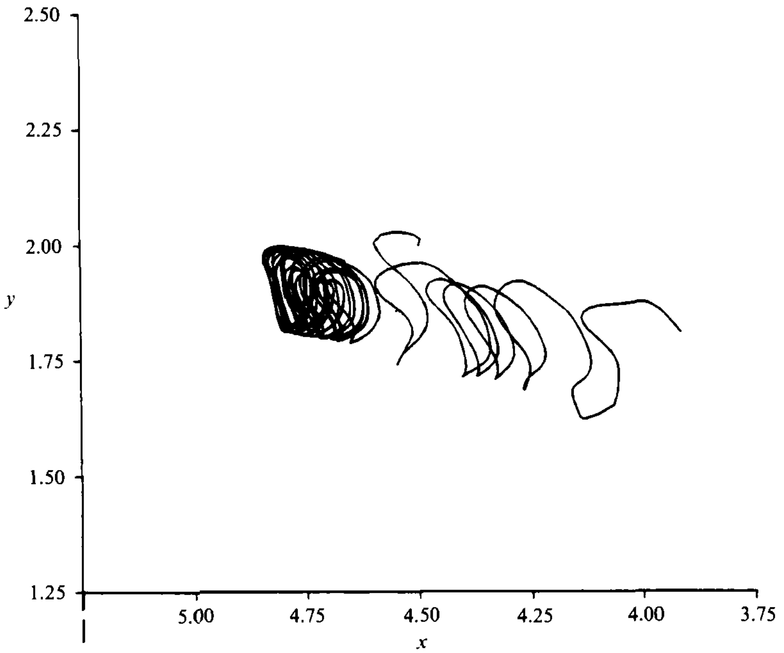

FIGURE 39. Side view of the vorticity lines surrounding the flux of figure 40.

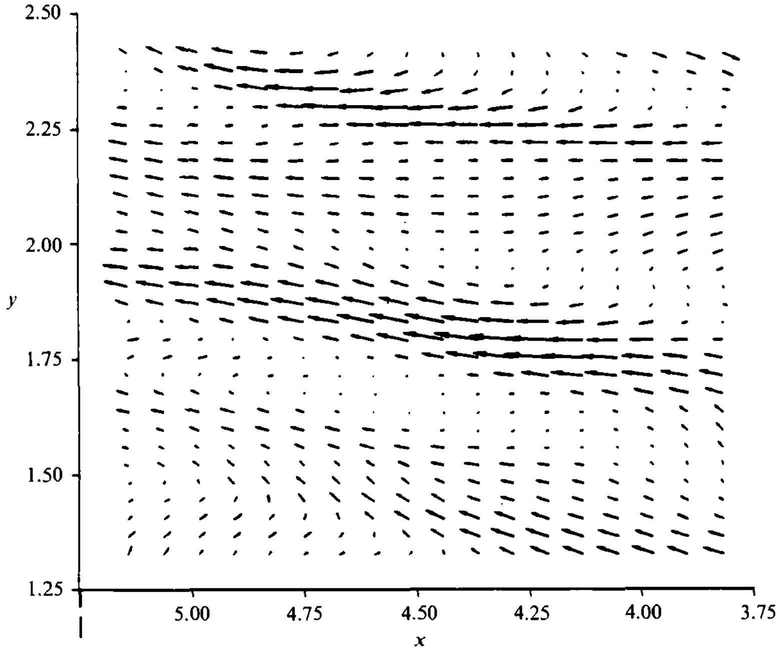

FIGURE 40. Velocity vectors in the mid-plane of the structure of figure 39.

rule). Furthermore, the velocity field in the vertical (x, y) mid-plane of the helix (figure 40) indicates that the CG fluid parcel moves in a direction consistent with the induced vorticity lines shown in figure 39. Figure 39 also provides a sense of scale of the helix; the vertical and streamwise dimensions of the computational domain are approximately 5 and 10 axis units.

We close our discussion of coherent vorticity structures by reviewing the physical mechanisms of their formation. We argued that the helical structure is induced by the motion of CG fluid parcels, whereas the velocity field associated with the hairpin structures produce DG fluxes. This proposition is consistent with the degree of nonlinearity in each case. For small $Ri < Ri_t$, the nonlinear interactions necessary for the formation of hairpins are significant (see §5.1). For example, spanwise vortex elements are perturbed into the principal strain directions by such interactions. Additional interactions contribute to self-inductive, reinforced pumping of the velocity field and ultimately in the formation of fluxes.

In the case of the helical structures nonlinear transfer is essentially absent (§5.3.3). Therefore the CG fluxes must be the result of linear processes which return fluid parcels toward their neutrally buoyant positions and, in so doing, induce the helical vorticity lines. In the presence of shear, the mean strain, rotation and stratification all act to constrain the path of the CG parcel.

8. Summary

The evolution and structure of homogeneous stably stratified turbulent shear flow have been investigated using direct numerical simulation. The simulation method solves the Boussinesq form of the Navier–Stokes equations using the pseudo-spectral technique of Rogallo (1981). In these simulations all relevant turbulent lengthscales were resolved. Hence, the solutions were restricted to low Reynolds numbers; effects of this have been assessed as far as possible.

8.1. *Richardson-number effects*

The effects of increasing Richardson number can be summarized as follows. The down-gradient Reynolds stress observed at low Richardson numbers leads to the production of streamwise velocity fluctuations. Some of this energy is redistributed to the spanwise and vertical components via pressure–strain interactions. The down-gradient vertical density flux demonstrates that the vertical kinetic energy associated with production events is being converted into potential energy. As the Richardson number increases the production and turbulent kinetic energy decrease.

At sufficiently large Richardson number buoyant fluid parcels eventually return toward their neutrally buoyant positions, releasing potential energy to vertical kinetic energy and causing a counter-gradient vertical density flux. Some of this vertical kinetic energy is redistributed to the streamwise kinetic energy which is decaying owing to the reversal of the Reynolds stress and therefore the production.

8.2. *Richardson-number classification*

The transition Richardson number Ri_t, differentiates between shear dominated and buoyancy dominated stably stratified shear flow. At the transition Richardson number the Reynolds stress and vertical density flux vanish at large dimensionless times, signalling a change from shear-driven down-gradient fluxes to counter-gradient oscillatory fluxes.

For Richardson numbers less than the transition value the anisotropy increases with increasing Richardson number. This is due to shear-induced production of streamwise velocity fluctuations and the conversion of vertical kinetic energy to potential energy. For Richardson numbers larger than the transition value the anisotropy decreases owing to the reversal in production and the release of potential energy to vertical kinetic energy. The ratio of potential energy to vertical kinetic energy also increases with increasing Richardson number up to the transition value then decreases slightly. Finally, the transition Richardson number apparently increases with increasing Reynolds number.

In the shear-dominated regime we observe the stationary Richardson number, Ri_s, at which the turbulent kinetic energy is nearly constant in time. The stationary Richardson number allows us to differentiate growing from decaying flow, a concept relevant to the estimation of vertical fluxes or dissipation rates based on a steady state assumption (see Van Atta 1985; Itsweire *et al.* 1990).

At low dimensionless shear rate the stationary Richardson number increases with increasing Reynolds number. This is because dissipation becomes less important as the Reynolds number increases and stronger stratification (a larger stationary Richardson number) is necessary to suppress the production of turbulence. At large Reynolds number the stationary Richardson number approaches the value (0.25) predicted by the linear inviscid stability analysis of Taylor (see Miles 1961). This value was also confirmed in the experiments of Rohr *et al.* (1988*b*).

At the stationary condition the stable stratification affects the turbulence growth rate primarily by suppressing production rather than directly reducing the turbulence growth rate. This effect should be modelled explicitly (see also Gerz *et al.* 1989). Finally, the energy spectra at the stationary Richardson number reveal that the lowest wavenumber modes gain energy in time owing to production whereas the higher wavenumber modes lose energy owing to the combined effects of suppressed production, reduced nonlinear transfer, and dissipation.

In the buoyancy-dominated regime the temporal behaviour of the fluxes and energetics scale with the Brunt–Väisälä frequency. Furthermore, the nonlinear spectral transfer of energy is severely suppressed, the vertical velocity and density are ± 180° out of phase, and the instantaneous density profiles reveal that the flow field is everywhere statically stable. These latter observations indicate that at large Richardson number the flow field is composed primarily of linear low-intensity buoyancy-driven counter-gradient motions.

8.3. *Effects of other parameters*

Significant initial potential energy produces a transient counter-gradient vertical density flux at small times which resolves the initial imbalance in the energy partition. The velocity field is also more energetic since turbulent kinetic energy is not expended to create potential energy. The developed flow is otherwise relatively insensitive to the initial ratio of potential energy to vertical kinetic energy. This result is consistent with that of Gerz & Schumann (1989). However, Hunt *et al.* (1988) showed that the unsheared case is sensitive to the initial potential energy.

As the Schmidt number is increased fluid parcels retain their density deviation from the ambient fluid, enhancing the effects of stable stratification. At large Richardson numbers ($Ri > Ri_t$) the increasing buoyant parcels are more effectively returned toward their neutral positions so that the vertical density flux reversal and the reduction in anistropy occur earlier.

8.4. *Coherent structure*

In the shear dominated case down-gradient fluxes are produced by movement of fluid through coherent hairpin-shaped vorticity lines, as previously shown by Rogers *et al.* (1986) in their study of unstratified homogeneous shear flow. In the buoyancy-dominated case counter-gradient fluid parcels induce helical vorticity lines while moving toward a position of neutral buoyancy. These counter-gradient fluxes are typically inclined 10°–20° from the horizontal. This is primarily due to the dominance of the streamwise velocity over the vertical velocity in the presence of shear and strong stratification.

The authors wish to thank Robert S. Roballo for making available the numerical method, Michael M. Rogers for providing advice on post-processing, Ching-Long Lin for assisting with post-processing, Stephen Monismith and Eric Itsweire for their advice on interpreting the data and Jill Nomura for her help in preparing the manuscript. In addition, the authors would like to thank the reviewers of an earlier version of this paper for their numerous constructive suggestions.

Financial support was provided by the Office of Naval Research (N00014-89-J-1909) and the Center for Turbulence Research at Stanford University. S.E.H. was also supported by a National Science Foundation Fellowship. The San Diego Supercomputer Center provided computational facilities.

REFERENCES

Batchelor, G. K. 1953 *The Theory of Homogeneous Turbulence.* Cambridge University Press.

Britter, R. E. 1988 Laboratory experiments on turbulence in density-stratified fluids. *Eighth Symp. of Turbulence and Diffusion. American Met. Soc., San Diego, California, April 26–29.*

Britter, R. E., Hunt, J. C. R., Marsh, G. L. & Snyder, W. H. 1983 The effect of stable stratification on turbulent diffusion and the decay of grid turbulence. *J. Fluid Mech.* **127**, 27.

Cooley, J. W. & Tukey, J. W. 1965 An algorithm for machine computation of complex Fourier series. *Math. Comp.* **19**, 297.

Deissler, R. G. 1961 Effects of inhomogeneity and of shear flow in weak turbulent fields. *Phys. Fluids* **4**, 1187.

Ellison, T. H. 1957 Turbulent transport of heat and momentum from an infinite rough plane. *J. Fluid Mech.* **2**, 456.

Gargett, A. E., Osborn, T. R. & Nasmyth, P. W. 1984 Local isotropy and the decay of turbulence in a stratified fluid. *J. Fluid Mech.* **144**, 231.

Gerz, T. 1989 Coherent structures in stratified turbulent shear flows deduced from direct simulations. In *Turbulence and Coherent Structures* (ed. M. Lesieur & O. Métais). Kluwer.

Gerz, T. & Schumann, U. 1989 Influence of initial conditions on the development of stratified homogeneous turbulent shear flow. *Finite Approximations in Fluid Mechanics*, vol. 2 (ed. E. Hirschel). Vieweg.

Gerz, T. & Schumann, U. 1991 Direct simulation of homogeneous turbulence and gravity waves in sheared and unsheared stratified flows. In *Turbulent Shear Flows 7* (ed. W. C. Reynolds), pp. 27–45. Springer.

Gerz, T., Schumann, U. & Elghobashi, S. E. 1989 Direct numerical simulation of stratified homogeneous turbulent shear flows. *J. Fluid Mech.* **200**, 563.

Gibson, C. H. 1980 Fossil temperature, salinity, and vorticity in the ocean. *Marine Turbulence* (ed. J. C. T. Nihoul) p. 221. Elsevier.

Head, M. R. & Bandyopadhyay, P. 1981 New aspects of turbulent boundary-layer structure. *J. Fluid Mech.* **107**, 297.

Herring, J. R. & Métais, O. 1989 Numerical experiments in forced stably stratified turbulence. *J. Fluid Mech.* **202**, 97.

Hinze, J. O. 1975 *Turbulence*, 2nd edn. McGraw-Hill.

Holt, S. E. 1990 The evolution and structure of homogeneous stably stratified sheared turbulence. PhD dissertation, Department of Civil Engineering, Stanford University.

Holt, S. E., Koseff, J. R. & Ferziger, J. H. 1989 The evolution of turbulence in the presence of mean shear and stable stratification. *Proc. Seventh Symp. on Turbulent Shear Flows*, Stanford University, Stanford, CA, Aug. 21–23.

Hopfinger, E. J. 1987 Turbulence in stratified fluids: A review. *J. Geophys. Res.* **92**, 5287.

HUNT, J. C. R. 1978 A review of the theory of rapidly distorted turbulent flows and its applications. *Fluid Dyn. Trans.* **9**, 121.

HUNT, J. C. R., STRETCH, D. D. & BRITTER, R. E. 1988 Length scales in stably stratified flows and their use in turbulence models. *Stably Stratified Flow and Dense Gas Dispersion* (ed. J. S. Puttock), p. 285. Clarendon.

ITSWEIRE, E. C. & HELLAND, K. N. 1989 Spectra and energy transfer in stably stratified turbulence. *J. Fluid Mech.* **207**, 419.

ITSWEIRE, E. C., HELLAND, K. N. & VAN ATTA, C. W. 1986 The evolution of grid-generated turbulence in a stably stratified fluid. *J. Fluid Mech.* **162**, 229.

ITSWEIRE, E. C., HOLT, S. E., KOSEFF, J. R. & FERZIGER, J. H. 1990 Direct numerical simulations of stably stratified sheared turbulence: Implications for oceanic mixing. *Proc. 1990 Summer Program, Center for Turbulence Res. Stanford University*, p. 161.

KÁRMÁN, T. VON. 1937 The Fundamentals of the statistical theory of turbulence. *J. Aero. Sci.* **4**, 131.

KOMORI, S., UEDA, H., OGINO, F. & MIZUSHINA, T. 1983 Turbulence structure in stably stratified open-channel flow. *J. Fluid Mech.* **130**, 13.

LAUNDER, B. E. 1976 Heat and mass transport. *Turbulence* (ed. P. Bradshaw). Topics in Applied Physics, vol. **12**, p. 232. Springer.

LIENHARD, V. J. H. & VAN ATTA, C. W. 1990 The decay of turbulence in thermally stratified flow. *J. Fluid Mech.* **210**, 57.

MÉTAIS, O. & HERRING, J. R. 1989 Numerical simulations of freely evolving turbulence in stably stratified fluids. *J. Fluid Mech.* **202**, 117.

MILES, J. W. 1961 On the stability of heterogeneous shear flows. *J. Fluid Mech.* **10**, 496.

MOIN, P. & KIM, J. 1985 The structure of the vorticity field in turbulent channel flow. Part 1. Analysis of instantaneous fields and statistical correlations. *J. Fluid Mech.* **155**, 441.

ORSZAG, S. A. 1969 *Phys. Fluids Suppl. II*, **12**, 250.

OZMIDOV, R. V. 1965 On the turbulent exchange in a stably stratified ocean. *Atmos. Ocean Phys.* **10**, 83.

RILEY, J. J., METCALFE, R. W. & WEISSMAN, M. A. 1981 Direct numerical simulations of homogeneous turbulence in density stratified fluids. *Non-linear Properties of Internal Waves* (ed. B. J. West). AIP Conf. Proc. Vol. **76**.

ROBINSON, S. K. 1990 Kinematics of turbulent boundary layer structure. PhD dissertation, Stanford University.

ROGALLO, R. S. 1981 Numerical experiments in homogeneous turbulence. *NASA Tech. Memo.* 81315.

ROGERS, M. M., MOIN, P. & REYNOLDS, W. C. 1986 The structure and modelling of the hydrodynamic and passive scalar fields in homogeneous turbulent flows. *Dept. Mech. Engng Rep* TF-25, Stanford University.

ROHR, J. J. 1985 An experimental study of evolving turbulence in uniform mean shear flows with and without stable stratification. PhD dissertation, University of California, San Diego.

ROHR, J. J., ITSWEIRE, E. C., HELLAND, K. N. & VAN ATTA, C. W. 1988*a* An investigation of the growth of turbulence in a uniform-mean-shear flow. *J. Fluid Mech.* **187**, 1.

ROHR, J. J., ITSWEIRE, E. C., HELLAND, K. N. & VAN ATTA, C. W. 1988*b* Growth and decay of turbulence in a stably stratified shear flow. *J. Fluid Mech.* **195**, 77.

SHIRANI, E., FERZIGER, J. H. & REYNOLDS, W. C. 1981 Mixing of a passive scalar in isotropic and sheared homogeneous turbulence. *Dept. Mech. Engng Rep.* TF-15, Stanford University.

SPALART, P. R. 1988 Direct simulation of a turbulent boundary layer up to $Re_\theta = 1410$. *J. Fluid Mech.* **87**, 61.

STEWART, R. W. 1969 Turbulence and waves in a stratified atmosphere. *Radio Sci.* **4**, 1289.

STILLINGER, D. C., HELLAND, K. N. & VAN ATTA, C. W. 1983 Experiments on the transition of homogeneous turbulence to internal waves in a stratified fluid. *J. Fluid Mech.* **131**, 91.

TAVOULARIS, S. & CORRSIN, S. 1981 Experiments in nearly homogeneous turbulent shear flow with a uniform mean temperature gradient. Parts 1, 2. *J. Fluid Mech.* **104**, 311.

TOWNSEND, A. A. 1976 *The Structure of Turbulent Shear Flow*, 2nd edn. Cambridge University Press.

TURNER, J. S. 1973 *Buoyancy Effects in Fluids*. Cambridge University Press.

VAN ATTA, C. W. 1985 Some challenges for modelling of turbulence and internal waves in stably stratified fluids. In *Macroscopic Modelling of Turbulent Flows and Fluid Mixtures* (ed. O. Pironneau). Springer.

VAN DYKE, M. 1982 *An Album of Fluid Motion*. Parabolic.

YOON, K. & WARHAFT, Z. 1990 The evolution of grid generated turbulence under conditions of stable thermal stratification. *J. Fluid Mech.* **215**, 601.